



Contents lists available at ScienceDirect

Journal of the Mechanics and Physics of Solids

journal homepage: www.elsevier.com/locate/jmps

A continuum thermodynamic framework for grain boundary motion



Ian Chesser^a, Tingting Yu^{b,c}, Chuang Deng^c, Elizabeth Holm^a,
Brandon Runnels^{d,*}

^a Department of Materials Science and Engineering, Carnegie Mellon University, Pittsburgh, PA 15213, United States

^b School of Materials Science and Engineering, Nanjing University of Science and Technology, Nanjing, China

^c Department of Mechanical Engineering, University of Manitoba, Winnipeg, MB, Canada

^d Department of Mechanical and Aerospace Engineering, University of Colorado, Colorado Springs, CO, United States

ARTICLE INFO

Article history:

Received 1 May 2019

Revised 1 November 2019

Accepted 11 December 2019

Available online 17 December 2019

ABSTRACT

In this work, we seek to explain grain boundary motion as a dissipative process within a thermodynamic framework inspired by continuum models for crystal plasticity. This allows for a unified explanation of phenomena such as motion by driving force, shear coupling, mode switching, and stagnation. We begin with a discussion of the kinematic requirements for grain boundary motion and the compatibility of grain boundary shear transformations. The model is based on the principal of minimum dissipation potential, where the “dual dissipation potential” is the energy loss per unit transformed volume as a result of interface motion. Several analytical examples are shown to demonstrate that this model consistently recovers multiple types of grain boundary migration behavior, indicating that the dissipation potential is an intrinsic grain boundary property. It is also shown that the model predicts the phenomenon of mode-switching, and that a “yield surface” can be constructed to relate mechanical loading to mode selection and yield. Molecular dynamics is then used to measure dissipation potential values (in particular the “dissipation energy”) for a wide number of boundaries. Rate-independent dissipation energies are determined for a crystallographically diverse set of 112 Ni grain boundaries using atomistic simulations with two distinct types of physical driving forces: an applied stress and energy jump. Agreement of dissipation energies across driving forces provides verification for the framework. The model's simplification of migration mechanisms provides a basis for unifying the observed varied grain boundary migration behavior subject to crystallography, driving force, and boundary conditions. Eventually, this framework can be used to develop experimentally calibrated models of grain boundary migration at the mesoscale.

© 2019 Elsevier Ltd. All rights reserved.

1. Introduction

Metals and ceramics are polycrystalline, meaning that they are composed of individual oriented crystals called grains separated by interfaces known as grain boundaries. Understanding grain boundary structure and motion is important for

* Corresponding author.

E-mail addresses: ichesser@andrew.cmu.edu (I. Chesser), Yu.Tingting@umanitoba.ca (T. Yu), Chuang.Deng@umanitoba.ca (C. Deng), eaholm@andrew.cmu.edu (E. Holm), brunnels@uccs.edu (B. Runnels).

<https://doi.org/10.1016/j.jmps.2019.103827>

0022-5096/© 2019 Elsevier Ltd. All rights reserved.

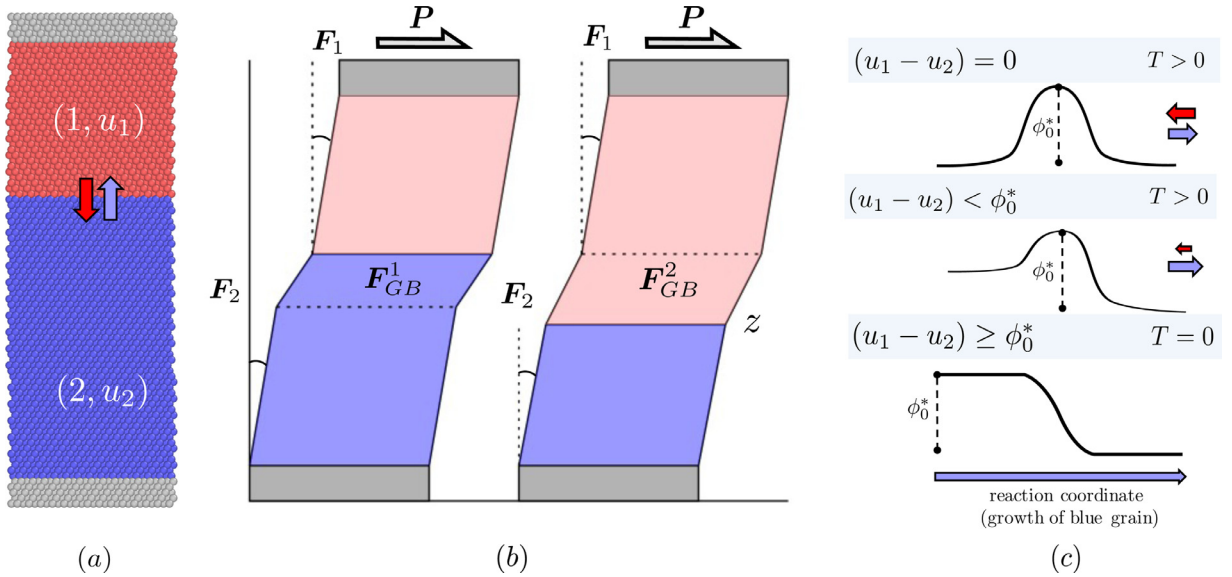


Fig. 1. Schematic illustrating the dissipative behavior of grain boundary motion (a) Grain boundary motion carries shear, which is understood in a continuum sense (b) as an eigendeformation F_{GB} corresponding to a particular mode (1 or 2 in diagram). The relative value of the dissipation energy ϕ_0^* (defined and discussed in detail in Section 2.3) to the driving force $(u_1 - u_2)$ determines the behavior of the boundary. (c) At 0K the boundary moves only if the driving force exceeds the dissipation energy (bottom row).

tuning a variety of properties in crystalline materials, including strength/ductility (Meyers et al., 2006), corrosion (Shi et al., 2016) and radiation resistance (Bai et al., 2010). Grain boundaries move significant distances during processes such as grain growth, recrystallization, and severe plastic deformation, often leading to microstructural coarsening (Rollett et al., 2004b; Rupert et al., 2009). In engineering applications, it is desirable to either prevent coarsening, retaining a strong material with small average grain size (Chookajorn et al., 2012), or promote coarsening to eliminate grain boundary area and create a material with a large average grain size and sharp texture (such as transformer steels (Raabe and Lücke, 1992)). In the thermodynamic limit of grain growth, all grain boundary area is eliminated and a single crystal is obtained. Grain growth usually stagnates well before the single crystal state is reached in a metastable state (Holm and Foiles, 2010). Recent experiments on grain growth in free hanging thin films that minimize stresses during annealing show significant coarsening that extends beyond the typical limits of abnormal grain growth and approaches the single crystal state (Jin et al., 2018). On the other hand, significant coarsening can be induced by stresses. Polycrystalline tantalum and molybdenum coarsen under an applied tensile load to a much greater extent than load free samples (Pedrazas et al., 2014; Worthington et al., 2013). The important supporting role of stress during grain growth, as well as the frequent coupling between crystal and grain boundary plasticity, motivates a mechanical treatment of grain growth.

Grain boundaries move irreversibly, dissipating energy into heat as they move. Grain boundary migration for a flat interface (Fig. 1a) is traditionally described using a gradient descent of the free energy multiplied by a scalar mobility M . The mobility thus encapsulates the relationship between rate of motion and the applied thermodynamic driving force F with units of a stress or equivalently free energy density. Here, the driving force is the derivative of free energy u of a planar interface with respect to its position x ; i.e.

$$V = MF \quad F = -\frac{\partial u}{\partial x}. \quad (1)$$

For curved boundaries with isotropic grain boundary energy and mobility, the driving force is $\kappa\gamma$, the product of mean curvature of the boundary (κ) and interface energy (γ). In the simplified case, most driving forces, including the curvature driving force, can be seen locally as an energy jump $(u_1 - u_2)$ across a flat grain boundary. Stress deserves special treatment as a driving force because it can couple to the burgers vector (shear component) of interface defects during interface migration.

Atomistic simulations have revealed a rich dependence of mobility on crystallography, temperature, and driving force. Olmsted surveyed the mobility of 388 grain boundaries in Ni via molecular dynamics energy jump driving force simulations and found variation in mobilities over four orders of magnitude with grain boundary crystallography (Olmsted et al., 2009b). Homer reported almost smooth variation of energy and mobility within grain boundary fundamental zones for these 388 Ni grain boundaries in a more recent study (Homer et al., 2015). Many of these grain boundaries also showed non-Arrhenius dependence of mobility on temperature, though this behavior remains unconfirmed experimentally (Cantwell et al., 2015; Humberson and Holm, 2017; Priedeman et al., 2017). In addition to strong crystallographic dependence, boundary migration is dependent on boundary conditions. This was illustrated in recent work by Thomas et al, in which the boundary conditions

for several boundaries were varied during energy jump-driven boundary motion via synthetic driving force (Thomas et al., 2017). It was observed that stresses induced by grain boundary motion can cause stagnation of boundary motion, uncontrolled boundary motion, or even repeated switching between modes in a “zig-zag” pattern reminiscent of deformation twinning in martensite (Ball, 2004; Ball and James, 1989). The wide variety of responses to driving force and boundary conditions suggests that boundary motion can be well explained from a continuum energetic perspective.

In experiments and simulations, certain flat grain boundaries in bicrystal samples are observed to be immobile until a sufficiently large shear stress is applied, at which point the grain boundary moves with a coupled normal and tangential displacement (Fig. 1b) (Cahn et al., 2006; Gorkaya et al., 2010; 2009; Li et al., 1953). When this deformation is a pure shear, it is characterized by the scalar shear coupling factor $\beta_n = v_n/\dot{z}_n$, the ratio between the shear velocity v_n and the orthogonal boundary velocity $\dot{z} = \frac{dz}{dt}$, where z is the scalar interface position. This coupling results in a permanent plastic deformation mediated by the motion of the grain boundary. Shear coupled grain boundary motion is generic to a wide variety of crystal structures, grain boundary geometries, and loading conditions – a compilation of experimental and molecular dynamics data can be found in Molodov and Molodov (2018) along with a history of the subject.

Atomistic simulations have shown that, just as shears can drive grain boundary motion, grain boundary motion can generate shears that do not require application of a stress (Homer et al., 2013). There are two fundamental types of driving forces for grain boundary motion: free energy jumps across the boundary and shear stresses resolved on the boundary (Han et al., 2018). Energy jump driving forces are discussed in depth in (Gottstein and Shvindlerman, 2009) and include, for example, energy jumps due to differences in stored elastic energy (Zhang et al., 2004) or dislocation density across the boundary (Rollett et al., 2004b). Chen and Srolovitz have found via molecular dynamics simulations that the dependence of shear coupling factor on temperature varies with driving force: energy jump, stress, and strain driven motion all can lead to different amounts of shear at finite temperature (Chen et al., 2019). This varied behavior has led to the argument that the shear coupling factor is not an “intrinsic grain boundary property” Chen et al. (2019).

At the atomistic level, deformations swept out by grain boundary migration are accommodated by *disconnections* (Han et al., 2018; Hirth, 1994). Disconnections are unit interface defects with coupled burgers vector and step height components (b_n, h_n). Each grain boundary has a countably infinite number of crystallographically available disconnection modes indexed by n , only a few of which are energetically competitive. Disconnections nucleate along grain boundaries and defect junctions and migrate to sweep out new volumes of energetically favored grains (Combe et al., 2016; Han et al., 2018). The shape change swept out by a large number of disconnections (b_n, h_n) of the same mode is represented by a lattice preserving deformation gradient $\mathbf{F}_{GB}^n \in GL(3, \mathbb{Z})$. Although disconnection theory provides a valuable understanding of the atomistic mechanism behind boundary migration, there is a need to link their aggregate behavior to reduced order thermodynamic models.

Recent advances in grain boundary modeling were made by Thomas *et al* to account for effects of competing modes, elasticity, and crystallographic anisotropy (Thomas et al., 2017). Otherwise, relatively little has been done at the continuum level to describe grain boundary motion beyond the simplified mobility-determined force-velocity relationship in Eq. 1. Within this context, no unified model predicting M from grain boundary geometry has emerged from a large body of experimental literature (Rollett et al., 2004a). This suggests that the simplified continuum model (Eq. 1) is fundamentally insufficient to describe the richness and complexity of grain boundary behavior. The fact that there are “mobile” vs “immobile” boundaries is a key indicator of the need for a more sophisticated model: for immobile boundaries M is undefined; for mobile boundaries M is an adequate descriptor, but then there is no distinction between highly mobile boundaries and boundaries that only become mobile after being subjected to a sufficiently high driving force.

In this work, the theory of crystal plasticity provides inspiration for developing a continuum dissipative framework for modeling the rich variety of grain boundary migration mechanisms and behaviors. In so doing, many of the concepts from crystal plasticity carry over cleanly to describe similar behavior mediated by boundary motion. Disconnections correspond to dislocations, disconnection modes (and consequently shear modes) to slip systems, driving force to critical resolved shear stress, and so on. This allows for grain boundary yield, rate-dependent boundary motion, rate hardening, and mode selection to be described in a continuum thermodynamic sense.

We begin with our continuum thermodynamic theory of planar grain boundary motion in the first section of the paper. The predominant focus is on the derivation of yield criteria (“rate-independent” flow rules) for grain boundary motion via comparison of a dissipation potential and thermodynamic driving force, demonstrating the important role of stress in energy driven motion. Next, we address the multiplicity of grain boundary transformations, and present a method for enumerating compatible shear transformations that is consistent with the disconnection model (Momprou et al., 2010). Finally, we propose two possible algorithms for computing dissipation energies with different driving forces: a stress and energy jump. Calculated dissipation energies for [1 0 0], [1 1 0], and [1 1 1] symmetric tilt boundaries are compared across driving force, and it is demonstrated that dissipation energy is an intrinsic grain boundary property that is invariant between loading scenarios. Finally, the results are contextualized in existing literature on grain boundary migration and plasticity.

2. Continuum thermodynamic theory of planar grain boundary motion

In this section we present a unified theory for energy-driven boundary motion in the language of continuum mechanics. Energetic models for dissipative processes such as plastic deformation frequently employ thermodynamic variational principles to select deformation modes that minimize free energy of a system.

Constitutive updates of internal variables such as plastic shear rates, or in our case, grain boundary migration rates, are reduced to a nonlinear optimization problem that admits complex deformation patterns as solutions. We propose a model analogous to crystal plasticity using the minimum dissipation framework (Carstensen et al., 2001; Hackl and Fischer, 2008; Kochmann and Hackl, 2011), wherein volumetric slip systems are replaced with boundaries, and slip rates with boundary velocities.

At this point it is useful to delineate different types of grain boundary motion in this work. In all cases, it may be safely assumed that there exists in every nontrivial grain boundary a characteristic amount of energy released during motion (per unit volume), which we will refer to as dissipation energy (ϕ_0^*), corresponding to a particular motion mechanism at 0 K. The set of possible motion mechanisms comprises a spectrum of dissipation energies or energy barriers. It is worth distinguishing the terms dissipation energy and energy barrier. Dissipation energy (ϕ_0^*) is a threshold value of the driving force required to suppress an intrinsic energy barrier to motion (E_0). While dissipation energy is an energy per unit volume, the energy barrier for interface motion is typically expressed as an energy per unit area. Mishin and Ivanov defined E_0 as the amplitude of a spatially periodic potential representing the incremental motion of a planar interface by a transformation height h (Ivanov and Mishin, 2008). In the Mishin-Ivanov model, dissipation energy and energy barrier are related by the interface transformation height as $\phi_0^* = \pi E_0/h$ (Ivanov and Mishin, 2008).

Stress and energy jump driving forces may suppress the spectrum of energy barriers at 0 K in different ways. While an energy jump driving force (such as an applied magnetic field) is expected to select the motion mechanism whose barrier vanishes first at 0 K, independent of the direction of the intrinsic GB shear, a shear stress gives preference to a motion mechanism that produces deformation parallel to the shear stress. In the case where the same motion mechanism is chosen by both a stress and energy jump driving force, the dissipation energy ϕ_0^* should not vary. Three cases can be considered for a single motion mechanism:

1. At finite temperature with no applied driving force, a grain boundary is equally likely to move in either direction (Fig. 1c, top) - we denote this as *random walk*.
2. A free energy difference across the grain boundary can come from many physical sources such as a difference in elastic energy density between grains or differences in dislocation density during recrystallization (Gottstein and Shvindlerman, 2009). When a free energy difference is applied across the boundary at finite temperature, the low energy grain is predicted to grow at the expense of the high energy grain (Fig. 1c, middle) - we call this *thermally activated motion*.
3. When the driving force exceeds the intrinsic energy barrier, then the boundary may be expected to move even in the athermal limit. Motion occurs when the energy dissipated during energy driven motion is equal to the intrinsic barrier to migration which we define as dissipation energy (ϕ_0^*) (Fig. 1c), bottom) - we refer to this as *energy-driven motion*.

Energy driven motion is relevant to experiments and simulations at finite temperature whenever a variation in driving force affects grain boundary migration mechanisms, such as grain boundary stagnation or zig-zag motion in (Thomas et al., 2017). In this work, we use dissipation energy to construct a continuum thermodynamic model of grain boundary motion. We focus predominantly on energy-driven motion in this work, establishing a model for rate independent boundary motion at 0 K that considers a variety of motion mechanisms and loading scenarios.

2.1. Kinematics: compatible grain boundary shear transformations

Deformation twinning is an example of permanent deformation accommodated by shear transformation associated with twin boundary motion. We expand on this concept by noting that the motion of every boundary must be associated with a deformation $\mathbb{F}_{GB} \in GL(3, \mathbb{Z})$. The deformation must (1) satisfy Hadamard compatibility with respect to the interface normal vector \mathbf{N} :

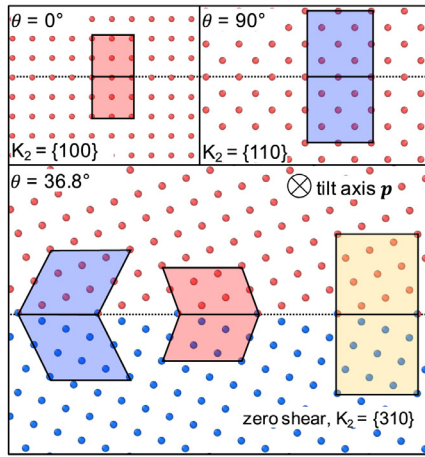
$$\exists \mathbf{a} \in \mathbb{R}^3 \text{ such that } \mathbf{F}_{GB} = \mathbf{I} + \mathbf{a} \otimes \mathbf{N}, \quad (2)$$

(2) be isochoric

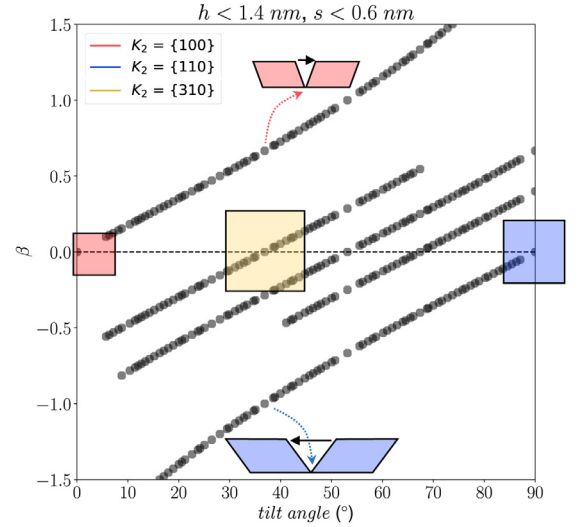
$$\det(\mathbf{F}_{GB}) = 1, \quad (3)$$

and (3) preserve crystallographic symmetry. (Precisely, given point sets $X, Y \subset \mathbb{R}^3$, where \mathbf{F}_{GB} corresponds to a mapping $\varphi: X \rightarrow Y$, then there also exists an isometry $\mathbf{R} \in SO(3): X \rightarrow Y$.) Because no nontrivial rotation satisfies compatibility, the first two requirements imply that $\mathbf{F} \neq \mathbf{R}$ except in the special case that $\mathbf{R} = \mathbf{F}_{GB} = \mathbf{I}$. This has the important implication that $\mathbf{F}_{GB} \neq \varphi$, i.e. the grain boundary shear *does not necessarily satisfy the Cauchy-Borne rule (CB)*. (Ericksen, 2008). (The CB rule assumes that all atoms within the lattice displace according to the average deformation of the continuum. Ericksen (2008)) This implies that the macroscopic deformation is accommodated crystallographically by a combination of CB-type displacements along with “shuffles,” so while φ preserves the crystallographic symmetry, it does not preserve ordering.

Restrictions (1) and (2) restrict the form of \mathbf{F}_{GB} to simple shear. By allowing for non-CB deformations, a wide (countably infinite) number of possible grain boundary shears are possible. Some nontrivial grain boundary shears do satisfy CB; this forms the basis for some recent work on deformation twinning Sun et al. (2018). However for most grain boundaries, non-CB deformations appear to be more likely mechanisms for transformation. It is also apparent that every boundary has



(a) Illustration of different possible \mathbf{F}_{GB} for different types of grain boundaries



(b) Shear coupling factors corresponding to different \mathbf{F}_{GB} s for symmetric tilt grain boundaries.

Fig. 2. Illustration of the many types of possible grain boundary shears including forward shear (blue) backward shear (red) and pure shuffle (yellow). (For interpretation of the references to color in this figure legend, the reader is referred to the web version of this article.)

a “shuffle-only,” zero-shear transformation corresponding to the shuffle transformation on the boundary’s coincident site lattice (Fig. 2a). This allows for the unification of shear-coupled and non-shear-coupled motion within the same kinematic framework.

The multiplicity of grain boundary shear transformations may be understood as the continuum representation of the action of different disconnection modes. At the atomic level, each compatible shear transformation corresponds to a disconnection type that nucleate at the grain boundary and migrates to sweep out new volume of energetically favored crystal. Eventually this results in the shear observed by \mathbf{F}_{GB} , in which the pure-shear off-diagonal component is exactly the coupling factor β_n (Fig. 2b). A coupling factor of zero corresponds to boundary motion without shear ($\mathbf{F}_{GB} = \mathbf{I}$), while an infinite coupling factor corresponds to pure grain boundary sliding (\mathbf{F}_{GB} incompatible). Pure grain boundary sliding is an incompatible transformation common in twist boundaries (where step and burgers vector components of disconnection are decoupled (Han et al., 2018)), and is not included in this present work. It should be noted that by “zero-shear” we refer strictly to shuffle-only, not combinations of equivalent shears. If multiple modes are energetically favorable for a single boundary, as is the case in zig zag or thermally activated motion, new values for shear coupling factor are accessible via combinations of modes. In this work, grain boundaries are assumed to move in a single energetically favored mode at any given point in time.

2.2. Special linearized elasticity

The mechanical process of simple grain boundary migration of interest include two stages of deformation: (i) grain boundary shear transformation, and (ii) the elastic response of applied loading. Grain boundary shear is clearly a “large” strain, but the elastic response is well within the linear regime. Therefore, we use a special formulation for elasticity that retains the convexity of linearized strain, but also preserves the notion of Hadamard compatibility.

Let a planar boundary parameterized by a nondimensionalized position $\hat{z} = z/L$ (where L is a characteristic length) move upwards such that Grain 1 is transformed into Grain 2, and that the compatible grain boundary shear transformation is \mathbf{F}_{GB} . Grains 1 and 2 have anisotropic elastic modulus tensors $\mathbb{C}_1, \mathbb{C}_2$ satisfying major and minor symmetry. Then the strain energy density for both grains are,

$$U_1(\mathbf{F}) = \frac{1}{2}(\mathbf{F} - \mathbf{I}) : \mathbb{C}_1(\mathbf{F} - \mathbf{I}), \quad U_2(\mathbf{F}) = \frac{1}{2}(\mathbf{F} - \mathbf{F}_{GB}) : \mathbb{C}_2(\mathbf{F} - \mathbf{F}_{GB}), \quad (4)$$

where \mathbf{F} is the deformation gradient, \mathbf{I} is the identity and $\mathbf{A} : \mathbf{B} = A_{ij}B_{ij}$. Although small strain is usually expressed in terms of the strain tensor $\boldsymbol{\epsilon}$, the minor symmetry of $\mathbb{C}_1, \mathbb{C}_2$ result in an equivalent expression. As stated above, using \mathbf{F} instead of $\boldsymbol{\epsilon}$ allows for a more natural treatment of large compatible deformations. It is important to emphasize that, despite appearances, the small strain approximation is still used, so many of the requirements for large strain models (such as material frame indifference) will not be satisfied.

2.2.1. Thermodynamic potentials and Clausius-Duhem inequality

The Helmholtz energy of a single crystal is defined here to be

$$A(\mathbf{F}, \mathbf{Q}, T) = U(\mathbf{F}) + u(\mathbf{Q}, T) \quad (5)$$

where U is the elastic strain energy density, \mathbf{Q} is a vector of internal variables, T is the temperature, and u is a thermodynamic potential that is independent of \mathbf{F} , such as a synthetic driving force. Here, and subsequently, all thermodynamic potentials are per unit volume unless stated otherwise. The Gibbs free energy is defined similarly via the Legendre transform,

$$G(\mathbf{P}, \mathbf{Q}, T) = \sup_{\mathbf{F}} \left[\mathbf{P} : \mathbf{F} - A(\mathbf{F}, \mathbf{Q}, T) \right], \quad (6)$$

where \mathbf{P} is the first Piola-Kirchhoff stress tensor. Using the special form of linearized elasticity, the Helmholtz and Gibbs energies have the explicit forms

$$A(\mathbf{F}, \mathbf{Q}, T) = \frac{1}{2}(\mathbf{F} - \mathbf{F}_{GB}) : \mathbb{C}(\mathbf{F} - \mathbf{F}_{GB}) + u(\mathbf{Q}, T) \quad (7)$$

$$G(\mathbf{P}, \mathbf{Q}, T) = \frac{1}{2}\mathbf{P} : \mathbb{C}^{-1}\mathbf{P} + \mathbf{P} : \mathbf{F}_{GB} + u(\mathbf{Q}, T), \quad (8)$$

where \mathbb{C}^{-1} is the compliance tensor. Assuming that grain 1 is the grain *above* \hat{z} and grain 2 is the grain below it, the combined Helmholtz energy for the bicrystal is:

$$A(\mathbf{F}_1, \mathbf{F}_2, \hat{z}, T) = \hat{z}A_2(\mathbf{F}_2) - \hat{z}A_1(\mathbf{F}_1), \quad (9)$$

where it is assumed that the deformation on either side of the boundary is uniform and affine, described by deformation gradients $\mathbf{F}_1, \mathbf{F}_2$. (Note that the subscripts 1 and 2 correspond to grains, and not deformation/disconnection modes.) The interface displacement \hat{z} can be interpreted as an internal variable. Following the Coleman-Noll procedure (Coleman and Noll, 1974), the thermodynamic driving force corresponding to the internal variable \hat{z} is

$$q = -\frac{\partial A}{\partial \hat{z}} = A_1(\mathbf{F}_2) - A_2(\mathbf{F}_1), \quad (10)$$

which is the nondimensional equivalent of the classical driving force in Eq. 1. The applied stress tensor decomposes $\mathbf{P} = \mathbf{P}^e + \mathbf{P}^v$, where $\mathbf{P}^e = dA/d\mathbf{F}$ is the purely elastic stress and \mathbf{P}^v is the stress corresponding to dissipation. These definitions enable the expression of a formal Clausius-Duhem inequality for planar boundary motion

$$\dot{\mathbf{F}} : \left(\mathbf{P} - \frac{dA}{d\mathbf{F}} \right) + \dot{\hat{z}} (A_1(\mathbf{F}_2) - A_2(\mathbf{F}_1)) \geq 0, \quad (11)$$

where $\dot{\mathbf{F}}$ is the time derivative of the of deformation gradient tensor.

2.3. Grain boundary dual dissipation potentials and the principle of minimum dissipation potential

Recall that the deformation gradients \mathbf{F}_{GB}^n enumerate boundary shear transformations undergone by the grain as the boundary passes through it. The deformation is irreversible and each has an energetic cost associated with the transformation. This energy can be represented using the so-called dissipation potential $\phi(q)$, where q is the driving force, and ϕ is the power (per unit volume), ostensibly dissipated as heat. The driving force is power-conjugate to the boundary velocity $\dot{\hat{z}}$, and so it is more natural to work with the dual dissipation potential $\phi^*(\dot{\hat{z}})$.

Definition 1. The grain boundary dual dissipation potential for the shear corresponding to mode n , $\phi_n^*(\dot{\hat{z}})$ is the dissipated power per unit volume associated with the transformation of a lattice from one orientation to another via the grain boundary transformation \mathbf{F}_{GB}^n . It is also the Legendre transform of the dissipation potential $\phi(q)$.

There exists one dual dissipation potential for each grain boundary mode, and thus, the selection of the mode is ostensibly determined by the mode with lowest dissipated energy. However, the difference between modes selected by traction-driven vs. displacement-driven boundary conditions show that the dual dissipation potential alone does not determine mode selection; rather, it is the combination of dual dissipation potential and deformation power that determine the optimal \mathbf{F}_{GB} . Conservation of energy dictates that the differential elastic energy loss due to boundary motion must precisely equal the energy dissipated; i.e.

$$\delta \dot{A} = -\delta \phi^* \quad (12)$$

If both are convex, then Eq. 12 has a variational expression. The variational formulation of the mechanics of dissipative systems was first introduced by Onsager (1931) as the principal of minimum dissipation potential. It has since been studied extensively and applied to plasticity (Carstensen et al. (2001); Hackl and Kochmann (2008); Mielke (2002); Ortiz and Repetto (1999), microstructure evolution (Mielke and Ortiz, 2008), and viscous solids (Roubíček, 2009; 2010), etc. We apply the principal of minimum dissipation potential to construct a variational model for grain boundary motion. (It should

be emphasized a variational model is primarily a mathematical convenience, and its existence does not necessarily imply a fundamental natural law (Cahn and Mullins, 1962; Hillert and Ågren, 2006; Martyushev and Seleznev, 2006; Zamberger et al., 2015).) The variational expression for which Eq. 12 is the solution is

$$\dot{z} = \arg \inf \min_n \left[\frac{d}{dt} A_n^*(\dot{z}, T) + \phi_n^*(\dot{z}) \right]. \quad (13)$$

$$A_n^* = \inf_{\mathbf{F}_1, \mathbf{F}_2} A_n(\mathbf{F}_1, \mathbf{F}_2, \dot{z}, T) \text{ subject to boundary conditions,} \quad (14)$$

where mode selection (minimization over n) is introduced as part of the model, not necessarily as a consequence of the principle of minimum dissipation potential.

The solution of Eq. 14 for A^* , \mathbf{F}_1 , \mathbf{F}_2 is equivalent to solving for linear momentum balance via the principal of minimum potential energy. Just as dual dissipation potentials in crystal plasticity determine slip behavior, the form of ϕ_n^* determines the evolution of the boundary. For instance, a boundary exhibiting power-law rate hardening would have a dual dissipation energy of the form

$$\phi_n^*(\dot{z}) = \phi_{n0}^* |\dot{z}| + \frac{1}{p} \phi_{np}^* |\dot{z}|^p, \quad (15)$$

where ϕ_{n0}^* , ϕ_{np}^* are constants and p is the power hardening exponent. (The units of ϕ_{np}^* are energy per unit volume per unit time to the p -th power.) It will be shown subsequently that if $p = 2$ and $\phi_{n0}^* = 0$, then $\phi_{n0}^* = 1/M$, the reciprocal of the ‘‘mobility.’’ In the ‘‘rate-independent’’ case where $\phi_{np}^* = 0$, the first coefficient ϕ_{n0}^* dictates the critical driving force necessary to initiate boundary motion - i.e. a yield stress. These parameters can be used to fit a model for ϕ_n^* that is capable of capturing a wide range of boundary behavior. It also allows for the treatment of ‘‘mobile’’ vs ‘‘immobile’’ boundaries. The parameter ϕ_{n0}^* is of particular interest as it allows for the quantification of boundary yield.

Definition 2. The grain boundary dissipation energy for mode n , ϕ_{n0}^* , is the energy per unit volume required to transform a crystal from one orientation to another via a grain boundary transformation \mathbf{F}_{GB}^n .

The dissipation energy is a property that is unique to each grain boundary, and is independent of the loading or boundary conditions to which the boundary is subjected. For the rate-independent case, transient simulations are not necessary to measure ϕ_0^* ; quasi-static simulations can be used (and, in fact, should be used) to measure this quantity. Special attention is given in this work toward the determination of the dissipation energy for each boundary. In the following section, the model will be applied to a selection of boundary conditions to illustrate the effect of the dual dissipation potential on mode selection and boundary evolution.

2.4. Examples

In this section, the minimum dissipation potential model for grain boundary motion is applied to a selection of simple loading conditions that are known to cause boundary motion. To streamline notation, a single mode is considered for all examples, and the sub/superscript n is dropped. For simplicity, the following form is used for the dual dissipation potential

$$\phi^*(|\dot{z}|) = \phi_0^* |\dot{z}| + \frac{1}{2} \phi_1^* |\dot{z}|^2 \quad (16)$$

Example 1 (Motion from applied driving force). Let the two grains be free from an applied mechanical load. A prescribed energy difference is applied to the two grains so that

$$A(\mathbf{F}_1, \mathbf{F}_2, z, T) = \hat{z} u_2 - \hat{z} u_1, \quad (17)$$

where u_1 , u_2 are constants. Practical examples include the application of a synthetic driving force in molecular dynamics simulations, or the creation of low-energy surfaces in thin materials. Substituting into the expression for minimum dissipation potential yields

$$\dot{z} = \arg \inf \min_n \left[\dot{z}(u_2 - u_1) + \phi_0^*(|\dot{z}|) \right] = \begin{cases} +\frac{1}{\phi_1^*} [(u_1 - u_2) - \phi_0^*] & +(u_1 - u_2) > +\phi_0 \\ -\frac{1}{\phi_1^*} [(u_1 - u_2) - \phi_0^*] & -(u_1 - u_2) < -\phi_0 \\ 0 & \text{else} \end{cases} \quad (18)$$

In the special case when $\phi_0^* \rightarrow 0$ (i.e. there is no yield criterion), then the evolution equation reduces to:

$$\dot{z} = \frac{1}{\phi_1^*} (u_1 - u_2), \quad (19)$$

which is the same form as Eq. 1, where $\phi_1^* = 1/M$, the reciprocal of grain boundary mobility. In the other special case where $\phi_1^* \rightarrow 0$ (i.e. infinite mobility), then the boundary velocity is either 0 or $\pm \infty$. This is analogous to elastic-perfectly-plastic behavior in crystal plasticity.

Example 2 (Stress-driven motion). We consider the case where the boundary is subjected to a uniform stress state \mathbf{P} . Because the solution is quasi-static (no dynamics are considered), the conservation of momentum jump condition requires that $[[\mathbf{P}]] = \mathbf{0}$ across the grain boundary. Accounting for the dual (applied stress) boundary condition, the problem becomes

$$\dot{\hat{z}} = \arg \inf_{\hat{z}} \left[\frac{\partial}{\partial \hat{t}} \left(\inf_{\mathbf{F}_1, \mathbf{F}_2} \left\{ \hat{z} (A_2(\mathbf{F}_2) - \mathbf{P} : \mathbf{F}_2) - \hat{z} (A_1(\mathbf{F}_1) - \mathbf{P} : \mathbf{F}_1) \right\} \right) + \phi_0^*(|\dot{\hat{z}}|) \right] \quad (20)$$

$$= \arg \inf_{\hat{z}} \left[\dot{\hat{z}} \left(G_2(\mathbf{P}) - G_1(\mathbf{P}) \right) + \phi_0^*(|\dot{\hat{z}}|) \right] \quad (21)$$

The general solution is

$$\dot{\hat{z}} = \begin{cases} +\frac{1}{\phi_1^*} (G_1(\mathbf{P}) - G_2(\mathbf{P}) - \phi_0^*) & + (G_1(\mathbf{P}) - G_2(\mathbf{P})) > \phi_0^* \\ -\frac{1}{\phi_1^*} (G_1(\mathbf{P}) - G_2(\mathbf{P}) - \phi_0^*) & - (G_1(\mathbf{P}) - G_2(\mathbf{P})) < -\phi_0^* \\ 0 & \text{else} \end{cases} \quad (22)$$

It is often the case that shear coupled motion occurs in boundaries for which there is no difference in elastic strain energy across the boundary. Therefore, it is instructive and useful to make the simplification that the two grains, though elastically anisotropic, do not exhibit a difference in strain energy under this particular loading. Mathematically, this can be stated as $\mathbf{P} \in \ker(\mathbb{C}_1^{-1} - \mathbb{C}_2^{-1})$. With this simplification, the expression for the interface velocity reduces to:

$$\dot{\hat{z}} = \begin{cases} +\frac{1}{\phi_1^*} [\mathbf{P} : (\mathbf{F}_{GB} - \mathbf{I}) - \phi_0^*] & +\mathbf{P} : (\mathbf{F}_{GB} - \mathbf{I}) > \phi_0^* \\ -\frac{1}{\phi_1^*} [\mathbf{P} : (\mathbf{F}_{GB} - \mathbf{I}) - \phi_0^*] & -\mathbf{P} : (\mathbf{F}_{GB} - \mathbf{I}) < -\phi_0^* \\ 0 & \text{else} \end{cases} \quad (23)$$

This piece-wise form indicates that for every mode there is a set

$$Y_n = \{ \mathbf{P} \in L(\mathbb{R}^3, \mathbb{R}^3), |\mathbf{P} : (\mathbf{F}_{GB}^n - \mathbf{I})| > \phi_0^*(\mathbf{F}_{GB} - \mathbf{I}) \}, \quad (24)$$

so that the boundary ∂Y_n defines a *yield surface* corresponding to that shear mode. The *total* yield surface (accounting for every possible shear mode) is given by the boundary of the intersection

$$\partial \left(\bigcap_n Y_n \right) \quad (25)$$

For symmetric tilt boundaries loaded with a pure shear stress P_{12} perpendicular to the tilt axis,

$$Y_n = \{ P_{12} \in \mathbb{R}, |P_{12} : \beta_n(\theta)| > \phi_0^*(\beta_n(\theta)) \} \quad (26)$$

where $\beta_n(\theta)$ is the coupling factor which depends on misorientation angle θ and disconnection mode n . An explicit formula for $\beta_n(\theta)$ is given in [Section 2](#).

In general, an elastic energy difference may contribute to grain boundary yield. For thermodynamically identical boundaries with zero elastic energy difference under a pure shear load, a mixed loading state with normal and shear components may break the thermodynamic symmetry of the system and induce an elastic energy difference across the boundary, depending on grain boundary geometry.

Example 3 (Displacement-driven grain boundary motion). We consider the case where a grain boundary is driven to move as the result of an imposed deformation. It has been observed that loadings of this type can cause initial movement of boundaries, but that the motion is eventually arrested. We seek to replicate this behavior with the continuum dissipation model.

Let Grain 1 occupy the region $L/2 > x_3 > z$ and Grain 2 the region $-L/2 < x_3 < z$, where x_3 is the coordinate normal to the boundary and $\hat{z} = z/L$, where z is the location of the boundary (initially zero), L is the height of the bicrystal, H^2 is the cross-sectional area, and $V = H^2 L$ the volume of the bicrystal. We impose a shear deformation on the bicrystal such that the overall (average) deformation gradient is given by \mathbf{F}_0 , where \mathbf{F}_0 is a simple shear.

A brief calculation shows that this constraint can be expressed as

$$\left(\frac{1}{2} + \hat{z} \right) \mathbf{F}_2 + \left(\frac{1}{2} - \hat{z} \right) \mathbf{F}_1 = \mathbf{F}_0 - \hat{z} \mathbf{F}_{GB}, \quad (27)$$

where \mathbf{F}_{GB} , as before, is the shear associated with grain boundary motion. The expression for the optimal Helmholtz energy is

$$A^*(\hat{z}) = \inf_{\mathbf{F}_1, \mathbf{F}_2} A(\mathbf{F}_1, \mathbf{F}_2, \hat{z}) \text{ subject to } \left(\frac{1}{2} + \hat{z} \right) \mathbf{F}_2 + \left(\frac{1}{2} - \hat{z} \right) \mathbf{F}_1 = \mathbf{F}_0 - \hat{z} \mathbf{F}_{GB} \quad (28)$$

where the Helmholtz free energy is

$$A(\mathbf{F}_1, \mathbf{F}_2, \hat{z}) = \left(\frac{1}{2} + \hat{z} \right) A_2(\mathbf{F}_2) + \left(\frac{1}{2} - \hat{z} \right) A_1(\mathbf{F}_1). \quad (29)$$

To enforce the kinematic constraint we introduce the Lagrange multiplier Λ :

$$A^*(\hat{z}) = \sup_{\Lambda} \inf_{\mathbf{F}_1, \mathbf{F}_2} A(\mathbf{F}_1, \mathbf{F}_2, \hat{z}) - \Lambda : \left\{ \left(\frac{1}{2} + \hat{z} \right) \mathbf{F}_2 + \left(\frac{1}{2} - \hat{z} \right) \mathbf{F}_1 - \mathbf{F}_0 + \hat{z} \mathbf{F}_{GB} \right\} \quad (30)$$

Stationarity for the $\mathbf{F}_1, \mathbf{F}_2$ gives

$$\Lambda = \frac{\partial A_1}{\partial \mathbf{F}_1} = \frac{\partial A_2}{\partial \mathbf{F}_2} \quad (31)$$

which, together with Eq. 27, is a solvable system for $\mathbf{F}_1, \mathbf{F}_2$. The exact solution in the general case is cumbersome, and it is therefore instructive to consider a reduced-order system. Let the $\mathbf{F}_1, \mathbf{F}_2$ be pure shear parameterized by γ_1, γ_2 , the grain boundary shear by γ_{GB} , and the imposed shear by γ_0 . Furthermore, let the crystals have elastic moduli μ_1, μ_2 such that the Helmholtz free energy is

$$A(\gamma_1, \gamma_2, z) = \frac{1}{2} \left(\frac{1}{2} + \hat{z} \right) \mu_2 \gamma_2^2 + \frac{1}{2} \left(\frac{1}{2} - \hat{z} \right) \mu_1 \gamma_1^2. \quad (32)$$

(We note that $\mu_1 \neq \mu_2$ implies anisotropy rather than differing material properties across the boundary.) Substituting this form into the reduced expressions for Eqs. 27 and 31, we find that

$$\gamma_1 = \frac{\mu_2(L\gamma_0 - z\gamma_{GB})}{\mu_1(L/2 + z) + \mu_2(L/2 - z)} \quad \gamma_2 = \frac{\mu_1(L\gamma_0 - z\gamma_{GB})}{\mu_1(L/2 + z) + \mu_2(L/2 - z)} \quad (33)$$

Substituting we have the expression for the minimum Helmholtz energy

$$A(\gamma_1, \gamma_2, z) = \frac{1}{2} \frac{\mu_1 \mu_2 (\gamma_0 - \hat{z} \gamma_{GB})^2}{\mu_1(1/2 + \hat{z}) + \mu_2(1/2 - \hat{z})}. \quad (34)$$

Introducing the following nondimensionalization

$$\hat{t} = \frac{t}{t_0} \quad \hat{\mu} = \frac{\mu_1}{\mu_2}, \quad \hat{A} = \frac{A}{\mu_1}, \quad \hat{\phi}^* = \frac{t_0 \phi^*}{\mu_1}, \quad (35)$$

(where a dot over a hatted variable implies differentiation with respect to \hat{t}). The nondimensionalized Helmholtz energy is

$$\hat{A}(\gamma_1, \gamma_2, \hat{z}) = \frac{(\gamma_0 - \hat{z} \gamma_{GB})^2}{\hat{\mu}(1 + 2\hat{z}) + (1 - 2\hat{z})}. \quad (36)$$

Applying the nondimensionalization to the minimum dissipation equation, we have

$$\dot{\hat{z}} = \arg \inf_{\hat{z}} \left[\frac{\partial \hat{A}}{\partial \hat{z}} \dot{\hat{z}} + \hat{\phi}^*(\dot{\hat{z}}) \right] \quad (37)$$

for which the stationarity condition gives

$$\frac{\partial \hat{A}}{\partial \hat{z}} + \frac{\partial \hat{\phi}^*}{\partial \dot{\hat{z}}} = 0. \quad (38)$$

Substituting Eq. 16, we arrive at the following differential equation for \hat{z} that can be integrated explicitly:

$$\frac{\partial \hat{A}}{\partial \hat{z}} + \phi_0^* \operatorname{sgn} \left(\frac{\partial \hat{z}}{\partial \hat{t}} \right) + \hat{\phi}_1^* \frac{\partial \hat{z}}{\partial \hat{t}} = 0. \quad (39)$$

A test case is considered in which the applied shear γ_0 is increased quasi-statically by incrementally increasing the amount of strain and allowing the system to equilibrate (Fig. 3). A value of 0.01 is used for ϕ_1^* , and the shear is applied incrementally to demonstrate the transient behavior of the model. Numerically integrating Eq. 39 and plotting the stress-strain curve shows that the system exhibits a distinct elastic-plastic behavior, which changes as a function of the dissipation energy $\hat{\phi}_0^*$. Note that the sawtooth-like behavior in the stress-strain curve (Fig. 3b) is the transient response to stairstepped loading, and should not be mistaken for stick-slip behavior.

The initial stairstepped region is elastic and recoverable, but once the driving force exceeds the dissipation energy, the boundary begins to move. Because the shear is stairstepped, the boundary is subjected to an initially high driving force, prompting rapid motion, but then the motion is arrested as the grains equilibrate. Eventually, the boundary reaches the end of the domain and can not move any further, and the bicrystal (which is now a single crystal) continues along an elastic curve.

Example 4 (Grain boundary stagnation). Grain boundaries that are subjected to fixed ends as well as an additional driving force (such as a synthetic driving force in MD) are sometimes observed to stagnate. To treat this scenario, we consider the formulation derived in Example 3, with the following added to the Helmholtz energy

$$\hat{A} \mapsto \hat{A} - \hat{z} \Delta \hat{u} \quad (40)$$

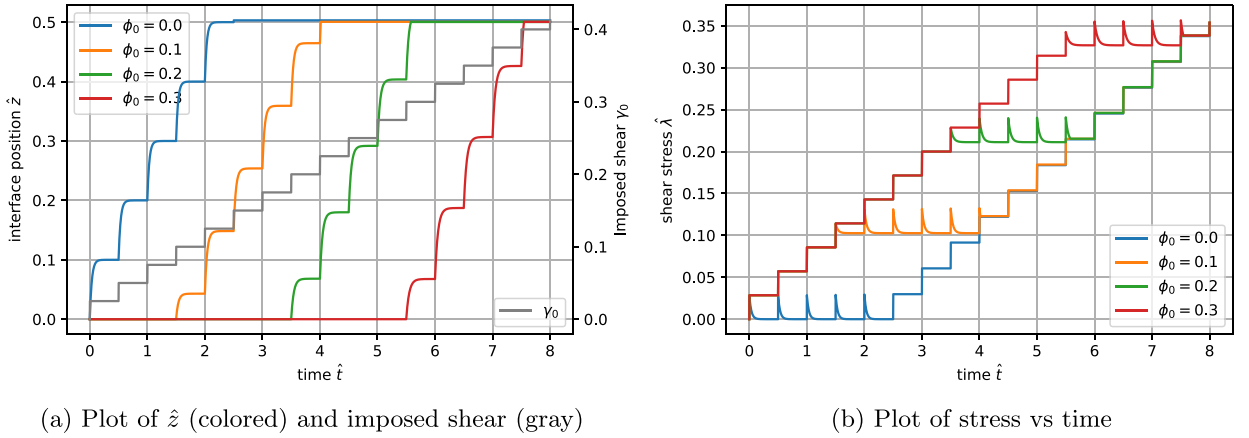


Fig. 3. Numerical integration of Eq. 39 for increasing imposed shear with varying dissipation energies. (a) plots the interface position with respect to time. (b) plots the stress strain curves (where time is a proxy for strain). Note that ϕ_0 is slightly less than the observed yield strain. This is the result of the elastic anisotropy ($\hat{\mu} \neq 1$).

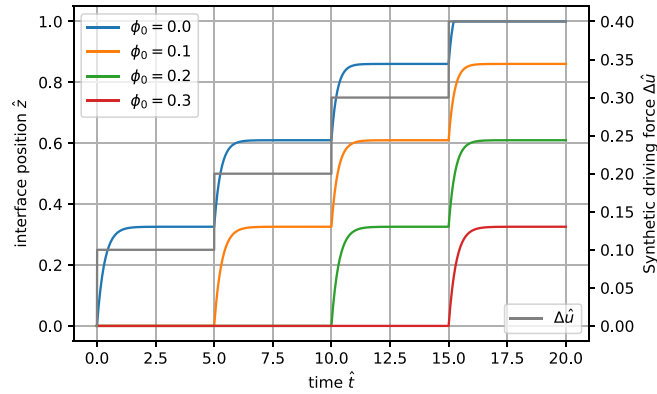


Fig. 4. Numerical integration of Eq. 41 for a stepped synthetic driving force. The driving force is applied and the boundary is allowed to equilibrate. The dissipation energy controls the threshold at which the boundary moves, as well as the stagnation location.

where $\Delta \hat{u} = 2(u_1 - u_2)/\mu_1$ is a nondimensionalized driving force. By repeating the calculations in Example 3 with this additional term, the evolution equation becomes

$$\frac{\partial \hat{A}}{\partial \hat{z}} + \hat{\phi}_0^* \operatorname{sgn} \left(\frac{\partial \hat{z}}{\partial \hat{t}} \right) + \hat{\phi}_1^* \frac{\partial \hat{z}}{\partial \hat{t}} = \Delta \hat{u}. \quad (41)$$

Eq. 41 is numerically integrated, with $\phi_1^* = 0.1$, for an incrementally increasing driving force and a selection of dissipation energies (Fig. 4). As expected, the dissipation energy controls the threshold for boundary motion, and determines the point at which the grain boundary stagnates. In this case, the blue curve ($\phi_0 = 0.0$) indicates the *true* equilibrium position for which the elastic energy is minimized. The other curves are restricted at an earlier point, and approach the position at which the dissipation energy is greater than the change in elastic energy.

3. Crystallographic enumeration of grain boundary shears for STGBs

Recall that, as a grain boundary migrates, it sweep out a macroscopic deformation composed of a sequence of deformations \mathbf{F}_{GB}^n , where n indexes crystallographically allowed disconnection modes. At finite temperature or with appropriate boundary conditions, grain boundaries may switch between modes or move in multiple modes simultaneously Thomas et al. (2017). In this section, we enumerate compatible \mathbf{F}_{GB}^n for yield of a symmetric tilt grain boundary (STGB) in a single mode.

STGBs are described by three parameters: a tilt axis $\hat{\mathbf{p}}$ (normalized with two degrees of freedom) and a misorientation angle θ . A STGB is created from a single crystal by symmetrically rotating upper and lower halves of the crystal by $\pm \theta/2$ about the rotation axis $\hat{\mathbf{p}}$. Since the grain boundary plane of an STGB (with normal $\hat{\mathbf{n}}$) is a mirror plane, STGBs are often referred to as twin boundaries. To satisfy compatibility, \mathbf{F}_{GB}^n must be a pure shear for flat STGB migration. Deformation is then

parameterized by a scalar coupling factor $\beta_n(\hat{\mathbf{p}}, \theta)$ that depends on STGB geometry. Each grain boundary has a countably infinite number of crystallographically accessible modes indexed by n .

Yield is determined by dissipation energy $\phi_0^*(\beta_n(\hat{\mathbf{p}}, \theta))$. In practice, only modes with relatively small shear and normal displacements will be energetically competitive. Fig. 2a shows shear coupling mode trajectories for $\langle 1\ 0\ 0 \rangle$ tilt boundaries in Al within a minimum shear and transformation height (for an FCC Al lattice). shear coupling factors $\beta(\theta)$ for $\hat{\mathbf{p}} = \langle 1\ 0\ 0 \rangle$ and varying n form approximately linear trajectories as a function of misorientation angle θ . Each *shear coupling mode trajectory* has a *zero shear reference state* (yellow shaded region) corresponding to a grain boundary with $\mathbf{F}_{CB} = \mathbf{I}$ and $\beta = 0$. At 0 and 90°, compatible shear transformations for zero shear reference states trivially map perfect crystals to perfect crystals and have zero dissipation energy. On the other hand, the zero shear reference state with $\mathbf{K}_2 = (3\ 1\ 0)$ has nonzero dissipation energy and corresponds to a pure shuffling transformation. A simple calculation shows that the coupling factors for each shear coupling mode trajectory are given by

$$\beta = 2 \tan\left(\frac{\theta - \theta^*}{2}\right), \quad (42)$$

where θ^* is angle corresponding to the zero shear reference state.

Each shear coupling mode trajectory is indexed by the second invariant plane of shear $\mathbf{K}_2 = \hat{\mathbf{p}} \times \mathbf{n}$ which is the same before and after a compatible shear transformation in a symmetric tilt boundary (Fig. 2b) Pitteri and Zanzotto (2002). \mathbf{K}_2 is an explicit crystallographic enumeration of the counting index n . Algorithm 1 gives a practical method for computing all compatible shear transformations for a given symmetric tilt boundary within a maximum shear and transformation height.

Algorithm 1 Enumeration of \mathbf{F}_{CB}^n for STGBs.

```

1: GB ← GBlist                                ▷ define sequence of grain boundaries with tilt axis  $\mathbf{p}$  and varying tilt angle  $\theta$  [53]
2: set ( $s_{\max}, h_{\max}$ )                       ▷ maximum allowed transformation shear and height
3: for ( $\theta, \mathbf{n}$ ) in GB do                       ▷  $\mathbf{n}$  is boundary plane direction [h k l] in crystal frame of grain 1
4:   for  $\theta^* \in [\theta_{\min}, \theta_{\max}]$  do
5:      $h = |K_1| \max\left[\cos\left(\frac{\theta - \theta^*}{2}\right), \sin\left(\frac{\theta - \theta^*}{2}\right)\right]$ 
6:      $s = 2h \tan\left(\frac{\theta - \theta^*}{2}\right)$ 
7:     if ( $s, h$ ) < ( $s_{\max}, h_{\max}$ ) then
8:       keep ( $s, z$ )
9:        $\mathbf{F}_{CB} = \mathbf{I} + s\mathbf{e}_1 \otimes \mathbf{e}_2$            ▷  $\mathbf{e}_1$  and  $\mathbf{e}_2$  are reference vectors in the lab frame
10:       $\beta = \frac{s}{h}$ 
11:     end if
12:   end for
13: end for

```

Our shear coupling mode enumeration results are consistent with the shear migration induced geometry (SMIG) model and the disconnection model (Han et al., 2018; Mompou et al., 2010). A similar expression for coupling factor can be found in Molodov and Molodov (2018), though zero shear reference states are not explicitly mentioned. In this work, we compute the energetic barriers to atomic motion during compatible shear transformations via atomistic simulation.

4. Computing dissipation energy via atomistic simulation

Dissipation energy $\phi_0^*(\beta_n(\hat{\mathbf{p}}, \theta))$ is computed for a wide range of symmetric tilt grain boundaries using two atomistic simulation methods with different driving forces: an energy jump driving force, also known as a synthetic driving force (SDF), and displacement driven shear (DDS). Atomistic models and simulation methods are described in detail below.

4.1. Bicrystal dataset

We consider migration of symmetric tilt grain boundaries (STGBs) in this work, using as an example grain boundary structures the 73 bicrystals with $\langle 1\ 0\ 0 \rangle$, $\langle 1\ 1\ 0 \rangle$, or $\langle 1\ 1\ 1 \rangle$ tilt axes in the 388 boundary Olmsted survey (Olmsted et al., 2009b). Later, we will also consider 39 grain boundaries with $\Sigma 3$ misorientation and varying boundary plane inclination. STGBs are a convenient choice for computing dissipation energy because they are observed to move in a variety of disconnection modes with nonzero shear coupling factor in experiments and molecular dynamics (MD) simulations (Cahn et al., 2006; Homer et al., 2015). STGBs are parameterized by a single degree of freedom, the misorientation angle θ . The subsequent motion mechanism of the grain boundary is characterized by the shear coupling factor β , which varies with disconnection mode for the same grain boundary. Note that the scalar mobility and shear coupling factor trajectories of these boundaries in Ni was surveyed in synthetic driving force simulations at 1000 K by Homer et. al in Homer et al. (2015). Tables 1–4 in Homer et al. (2015) provide a convenient tabulation of boundary crystallography, energy, and mobility for this dataset.

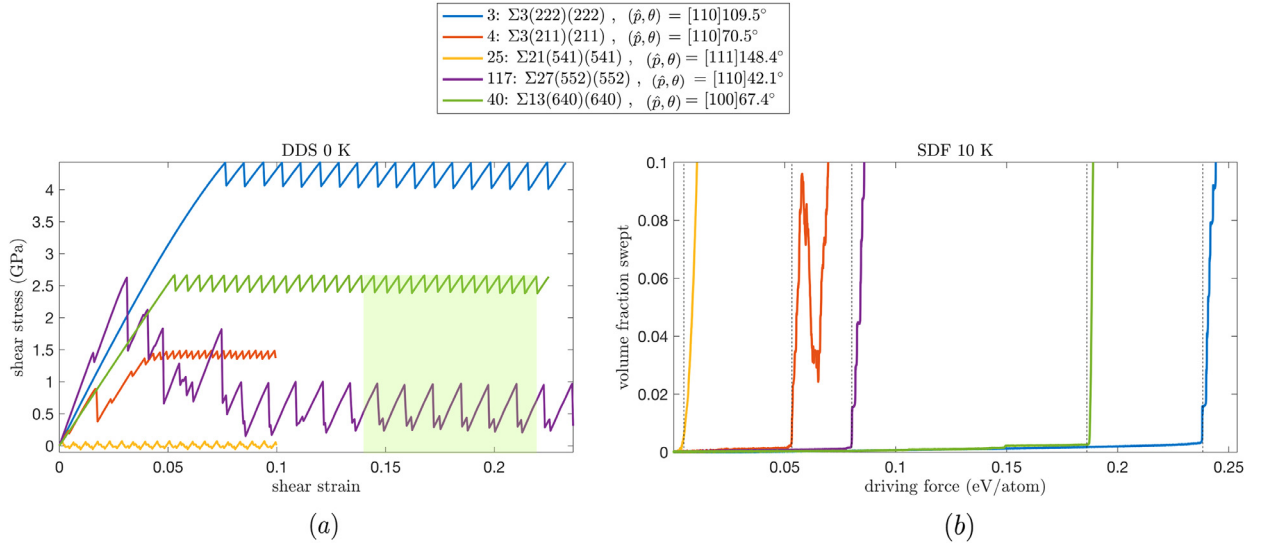


Fig. 5. (a) Calculation of dissipation energy using displacement-driven stress-strain curves. (b) Calculation of dissipation energy using a ramped synthetic driving force.

All atomistic bicrystal models satisfy periodic boundary conditions in the y-z interface plane and have free surfaces along the x direction normal to the grain boundary plane. The grain boundary energy of each structure is minimized over translational microscopic degrees of freedom, as described in [Olmsted et al. \(2009a\)](#) using the Foiles Hoyt EAM Ni interatomic potential ([Foiles and Hoyt, 2006](#)). To survey the effect of interatomic potential on dissipation energy, we also simulate migration of a set of Al STGBs from the Tschopp survey [Tschopp and McDowell \(2007\)](#) using the Mishin EAM Al potential ([Mishin et al., 2001](#)). For Ni boundaries, we use the same numbering scheme as the original Olmsted survey (see supplementary info of [Olmsted et al. \(2009a\)](#)). All Ni bicrystal structures have dimensions larger than 16 nm in the interface plane normal direction with cross sections larger than $3 \times 3 \text{ nm}^2$. Al bicrystal structures are comparatively thin in the direction of the tilt axis, with only one or two periodic repeats, but typically have dimensions larger than 5 nm in the direction of shear perpendicular to the tilt axis and larger than 16 nm in the plane normal direction.

4.2. Measuring dissipation energy via displacement driven shear simulations

During DDS simulations, a pure shear strain is applied to each bicrystal model by displacing fixed slabs at the top and bottom of the bicrystal in opposite directions along the z direction in the plane of the boundary. Note that the z direction is perpendicular to the tilt axis along the y direction, and that in general the direction of shear in the boundary plane may impact coupling mode ([Molodov and Molodov, 2018; Yin et al., 2018](#)). Displacement of both slabs in steps of 0.04 Å (per slab, 0.08 Å total) is accompanied by a conjugate gradient energy minimization ([Grippe and Lucidi, 1997](#)) at 0 K with force tolerance of 10^{-8} eV/Å and dimensionless energy tolerance 10^{-8} in LAMMPS ([Plimpton, 1995](#)). All bicrystals undergo 500 displacement steps, or 4 nm total shear displacement. Total shear strain varies with simulation box size for each bicrystal. At sufficiently large shear strains, all grain boundaries yield via plastic deformation. The grain boundaries surveyed, even among tilt boundaries, show a diverse array of plastic deformation mechanisms, including disconnection motion, grain boundary sliding, full and partial dislocation emission, and combinations thereof. Since F_{GB}^n is only well defined for combined normal migration and grain boundary sliding (disconnection motion), we only consider grain boundaries that yield via disconnection nucleation and motion. In the discussion that follows, we develop a procedure for filtering stress strain data so that we only keep data corresponding to disconnection motion. Finally, we discuss a method for measuring dissipation energy from stress strain curves.

A variety of stress strain curves for different bicrystal geometries are shown in [Fig. 5a](#). Out of the five boundaries, only three have sawtooth stress strain behavior over the full range of plastic deformation. A sawtooth plastic wave is a necessary but insufficient condition for plastic deformation via disconnection motion. Boundary 4, for example, commonly known as the incoherent twin boundary with (1 1 2) boundary planes, has a sawtooth plastic wave for shear strains larger than 0.04, but yields via extension of Shockley partial dislocations from the grain boundary into the bulk crystal at a strain of 0.015. An initial stress drop after dislocation nucleation is followed by a hardening regime and a sawtooth stress-strain regime corresponding to mixed disconnection and bulk dislocation motion. We do not consider mixed data, as in this case, which contains dislocation activity in bulk grains. Boundary 117, however, despite showing an initial regime of grain boundary sliding marked by irregular stress drops, does produce usable sawtooth stress strain data corresponding to disconnection motion for shear strains larger than 0.12. In this case, a steady state is reached without generating bulk dislocation content.

In summary, stress strain data is admissible for measurement of dissipation energy if a plastic steady state is reached which is sawtooth and free of defects in the bulk grains. Four out of five of the boundaries in Fig. 5a provide usable stress strain windows for dissipation energy measurement.

Dissipation energy (ϕ_0^*) is computed from admissible stress strain data using the following formula

$$\phi_0^* = \frac{1}{f_V} \int_{\epsilon_{i,p}}^{\epsilon_{f,p}} \boldsymbol{\sigma} : d\boldsymbol{\epsilon} \approx \frac{1}{f_V} \boldsymbol{\sigma}_y : (\boldsymbol{\epsilon}_{f,p} - \boldsymbol{\epsilon}_{i,p}). \quad (43)$$

where f_V is the volume fraction of energetically favored grain swept out by the moving grain boundary, $\boldsymbol{\epsilon}$, $\boldsymbol{\sigma}$ are the stress and strain tensors, $\boldsymbol{\epsilon}_{i,p}$ and $\boldsymbol{\epsilon}_{f,p}$ are arbitrarily chosen initial and final plastic strains (both greater than the yield strain) and $\boldsymbol{\sigma}_y$ is the yield stress. The proof of this relation is as follows. We begin by considering the quantity

$$V \int_{\epsilon_{i,p}}^{\epsilon_{f,p}} \boldsymbol{\sigma} : d\boldsymbol{\epsilon} \quad (44)$$

where V is the volume of the bicrystal. If the measured strain causes the boundary to move from h_i to h_f , then

$$\boldsymbol{\epsilon} = \boldsymbol{\epsilon}_e + \frac{h}{L} \boldsymbol{\epsilon}_{GB}, \quad (45)$$

where $\boldsymbol{\epsilon}_e$ is the elastic component of the strain, $\boldsymbol{\epsilon}_{GB}$ is the grain boundary shear strain (a constant), and L is the height of the bicrystal. Because the boundary has fully yielded, the elastic strain does not change. Consequently, the differential element of strain in this region is

$$d\boldsymbol{\epsilon} = \boldsymbol{\epsilon}_{GB} \frac{dh}{L}. \quad (46)$$

Substituting (46) into (44) returns

$$V \int_{h_i}^{h_f} (\boldsymbol{\sigma} : \boldsymbol{\epsilon}_{GB}) \frac{dh}{L} = A \Delta h (\boldsymbol{\sigma} : \boldsymbol{\epsilon}_{GB}) \quad (47)$$

where $A = V/L$ is the area of the boundary. We now change to the convention of special linearized elasticity (see Section 2.2), such that $\boldsymbol{\sigma} \mapsto \mathbf{P}$ and $\boldsymbol{\epsilon}_{GB} \mapsto \mathbf{F}_{GB} - \mathbf{I}$. Then (47) becomes

$$A \Delta h (\mathbf{P} : (\mathbf{F}_{GB} - \mathbf{I})) \quad (48)$$

Assuming (without loss of generality) that the boundary moves upwards, we have from (23)

$$\mathbf{P} : (\mathbf{F}_{GB} - \mathbf{I}) - \phi_0^* = \phi_1^* \dot{z} \quad (49)$$

If the boundary is moved quasi-statically, then this reduces to

$$\mathbf{P} : (\mathbf{F}_{GB} - \mathbf{I}) = \phi_0^* \quad (50)$$

This, in combination with (48) and (44), results in the final expression

$$\phi_0^* = \frac{V}{A \Delta h} \int_{\epsilon_{i,p}}^{\epsilon_{f,p}} \boldsymbol{\sigma} : d\boldsymbol{\epsilon} \quad (51)$$

where $A \Delta h / V = f_V$, proving the first equality in Eq. 43. The second (approximate) equality in Eq. 43 follows from the elastic-perfectly-plastic approximation, $\boldsymbol{\sigma} \approx \boldsymbol{\sigma}_y$

The calculation of $\boldsymbol{\sigma}_y : (\boldsymbol{\epsilon}_{f,p} - \boldsymbol{\epsilon}_{i,p})$ is shown pictorially as the area of the green box in Fig. 5a. Plastic work is approximated as the rectangular area under the plastic part of the stress strain curve, and is normalized by transformed volume fraction f_V to obtain ϕ_0^* . Computing f_V requires information about normal displacement of the boundary that is not contained in the stress strain curve. f_V is computed in a separate post-processing step by tracking the average position of the grain boundary via the centrosymmetry parameter. The shear coupling factor β is computed by dividing the known total shear displacement by normal migration distance.

Although Eq. 43 correctly captures ϕ_0^* for a specific stress-strain curve, it is important to note that the stress-strain curve will be simulation size-dependent. In fact, realistic boundary migration can, in general, exhibit large disconnection structures that require a sizeable simulation domain to resolve (Race et al. (2015)). Therefore, the calculated value for ϕ_0^* can only be considered accurate insofar as the computational bicrystal is representative of a real boundary. However, even with a small simulation size, it is possible to approximate ϕ_0^* . In the boundaries considered here, the effect of the simulation size (normal to the boundary) was determined. By incrementally increasing the length of the simulation, the sawtooth stress strain curve converges to an elastic perfectly plastic stress strain curve in the limit of infinitely large system size normal to the GB plane (Fig. 6). Apparently, in the limit, the average yield stress converges to peak yield stress as the elastic strain increment associated with each stress drop approaches zero (Ivanov and Mishin, 2008; Mishin et al., 2007). Therefore, by integrating the maximum stress instead of the average stress, the dissipation energy is approximated for a simulation cell that is infinite in the grain boundary normal direction. A similar process can (and should) be used to study the effects in the limit of in-plane simulation size; however, the computational cost of such a study is considerable and is outside of the scope of the present work.

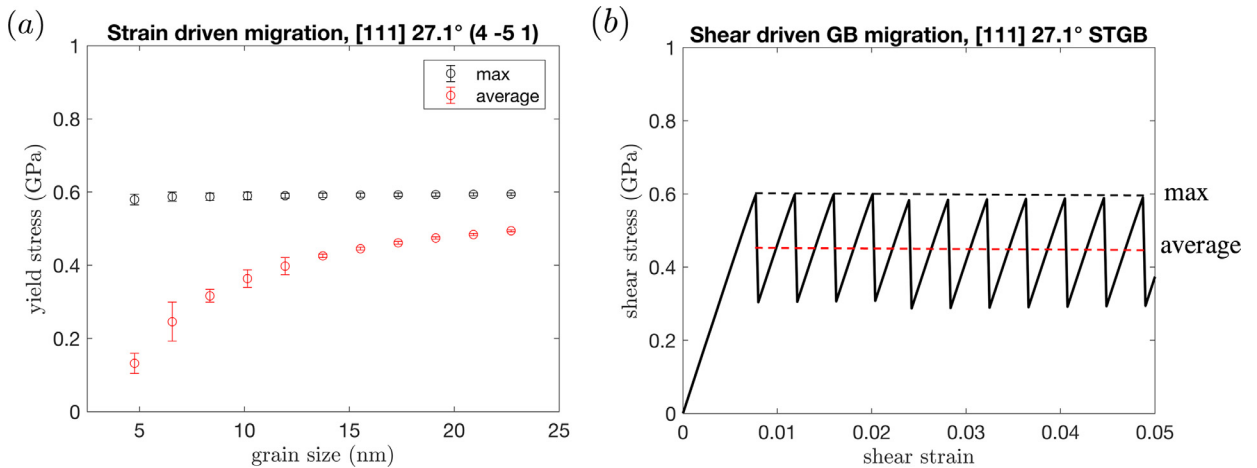


Fig. 6. (a) Average stress converges to yield stress as system size increases normal to the GB plane (b) Definition of average and yield stress for an example stress strain curve.

4.3. Measuring dissipation energy via synthetic driving force simulations

The SDF method applies a free energy jump across the grain boundary which favors growth of the low energy grain. We seek the critical driving force (units of GPa) at which the grain boundary starts to move, and therefore ramp the magnitude of the synthetic driving force upward from zero until a critical yield stress is reached. By [Example 1](#), this critical yield stress is equal to dissipation energy for the selected grain boundary migration mechanism for rate-independent motion.

We use the SDF implementation of Janssens that is freely available in the misc package of LAMMPS ([Janssens et al., 2006](#)). Each sample is annealed in an NVT ensemble at 10 K for 50 ps prior to application of a driving force. Following ([Deng and Deng, 2017](#)), an energy of $\frac{\delta E}{2} = 0.00001$ eV/atom is added to each atom every 0.05 ps, corresponding to a SDF ramp rate of 0.2 meV/ps. Rate dependency is a concern in extracting cutoff stress values from finite temperature simulations. It is shown in ([Deng and Deng, 2017](#)) that a ramp rate of 0.2 meV/ps is sufficiently slow for convergence of yield stress for a $\Sigma 5$ boundary at 10 K in an NVT ensemble.

Boundaries with migration mechanisms that generate bulk defect content are not considered, equivalent to our filtering procedure for stress driven data. [Fig. 5b](#) shows boundary position (volume fraction transformed) as a function of driving force for five grain boundaries. All boundaries move at a critical driving force equal to dissipation energy. Boundary 4, as in the DDS simulations, nucleates Shockley partials during motion, giving rise to an apparent reversal in motion direction, and is not considered further. The other four plotted boundaries give usable data.

The volume average of the order parameter associated with the driving force is used to dynamically track normal displacement along the x direction during SDF simulations. Shear displacements along y and z directions are monitored by tracking the displacements of two free slabs at the top and bottom of the bicrystal.

5. Results and discussion

We compare dissipation energies computed with stress (DDS) and energy jump (SDF) driving forces across $\langle 1\ 0\ 0 \rangle$, $\langle 1\ 1\ 0 \rangle$, and $\langle 1\ 1\ 1 \rangle$ symmetric tilt grain boundaries. By [Example 1](#), the yield surface for an energy jump driving force is simply the envelope of compatible shear transformations (disconnection modes) with minimum dissipation energy. By [Example 2](#), the yield surface for stress driven motion is constructed by dividing the dissipation energy $\phi_{0,n}^*$ of a given disconnection mode (b_n, h_n) by its coupling factor $\beta_n = \frac{b_n}{h_n}$.

5.1. Comparison of dissipation energy across driving forces

$[1\ 0\ 0]$ tilt boundaries are the canonical class of boundaries for studying shear coupled grain boundary migration in both simulations and experiments and, as such, are an important test case for our energetic framework for grain boundary mode selection. [Fig. 7](#) comprises the main simulation result of this work: coupling factor and dissipation energy trajectories give an energetic argument for mode switching as a function of grain boundary geometry for two driving forces. Where coupling factor values agree across driving force, dissipation energy values also agree well. $[100]$ tilt boundaries are shown to migrate in two distinct shear coupling modes across a range of tilt angles, consistent with experimental observations and prior simulation work. The transition between the $K_2 = (100)$ and $K_2 = (110)$ mode is accompanied by a change in sign of coupling factor. The $(1\ 0\ 0)$ mode is energetically favored for boundaries with relatively low tilt angles, while the $(1\ 1\ 0)$ mode is favored for large tilt angles. The critical mode switch angle is sensitive to driving force, and some boundaries in

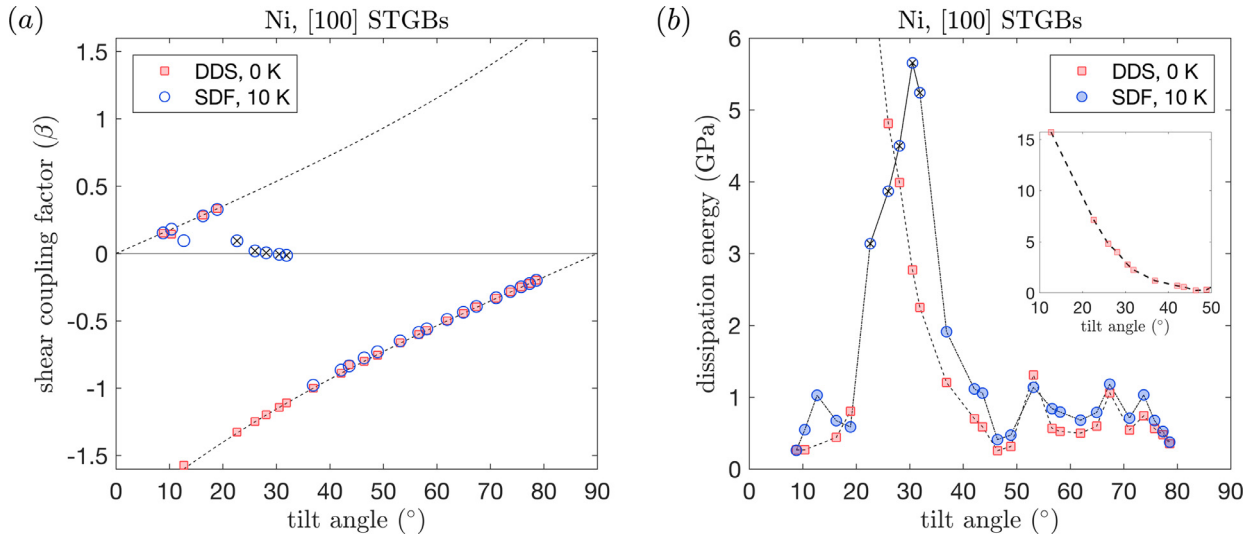


Fig. 7. (a) mode selection for two types of driving force: a shear displacement (DDS, red) and energy jump (SDF, blue). For points plotted with x, vacancy ejection is observed behind moving boundary. (b) Dissipation energies for two types of driving forces. The inset shows dissipation energies for the (1 1 0) mode which monotonically increase with increasing shear. (For interpretation of the references to color in this figure legend, the reader is referred to the web version of this article.)

the SDF simulations have near zero shear coupling factors that do not fall onto either coupling factor trajectory. We return to this exception below, but first comment on the directionality of grain boundary motion with applied driving force.

When the same pure shear load is applied to bicrystals with misorientation angles θ_1 and θ_2 below and above some mode switch angle $\theta_{(100) \rightarrow (110)}^*$, the boundary will migrate in opposite directions. When the same energy jump driving force is applied to boundaries with positive and negative shear coupling factor, the grain boundary will move in the same direction but with opposite sense of shear. Mode switching for a single grain boundary with a change in coupling factor will result in a reversal of motion for a stress and zig zag motion for a synthetic driving force: the shape change associated with grain boundary migration is sensitive to driving force.

Dissipation energies that correspond to equivalent shear coupling modes across DDS and SDF simulation agree closely. We denote data points with consistent coupling factors across driving force as *equal mode*. If different disconnection modes are selected by SDF and DDS for the same grain boundary, as is the case in the range 22–35°, we do not expect dissipation energies to agree across driving force, and data points are labeled *off mode*. Off mode data are plotted with X symbols. A mechanism oriented discussion of off-mode data points can be found at the end of this section. The differences in dissipation energies across driving force $\phi_{0,n,SDF}^* - \phi_{0,n,DDS}^*$ for $\langle 1\ 0\ 0 \rangle$ tilt boundaries are less than 300 MPa, with the exception of boundaries at tilt angles of 36.9, 42.1, and 43.6° which have errors between 0.5–1 GPa. Possible sources of error are discussed in Section 5. All dissipation energies are tabulated in the supplementary information. We proceed to compare the shape of dissipation energy curves for both driving forces across tilt angles.

In analogy to grain boundary energy, we separate dissipation energy behavior into low and high angle regimes. Since the grain boundaries at 0 and 90 degrees are trivially perfect crystals (with (1 0 0) and (1 1 0) boundary planes), we expect a minimum dissipation energy of zero at these angles. Recall that zero dissipation energy corresponds to the zero shear identity transformation $F_{GB}^n = I$ that involves no atomic displacement for a perfect crystal. For low angle grain boundaries (LAGBs) with misorientation angles within 15 degrees of a perfect crystal, we expect a gradual rise in dissipation energy from zero. For both driving forces, dissipation energies are observed to increase for three LAGBs from 8.8 to 12.7° and four boundaries from 78.4 to 73.7°. The latter range extends beyond the typical angular regime considered to be low angle. Apparently, dissipation energies decay to small values near zero in the range 0 to 8.8 and 78.4 to 90° for these Ni boundaries. LAGB behavior is sensitive to interatomic potential, as shown by the LAGB dissipation energy behavior for the Al $\langle 1\ 0\ 0 \rangle$ dataset for the $K_2 = (110)$ mode in Fig. 8a. A linear dissipation regime comprising seven Al data points from 73 to 85° extrapolates to zero dissipation energy at 90°. Determining the functional form of dissipation energy decay for LAGBs across interatomic potentials and, in particular, whether a Read-Shockley type rule exists, is an open problem.

High angle grain boundaries (HAGBs) with a $\langle 1\ 0\ 0 \rangle$ tilt axis form a nonconvex dissipation energy surface for the (1 1 0) mode. Locations of minima and maxima for HAGB dissipation energies agree across driving force as well as the Ni and Al interatomic potentials compared via DDS simulations in this work. The locations of minima and maxima appear to be independent of driving force and interatomic potential, suggesting a strong dependence of dissipation energy on grain boundary geometry for the same coupling factor trajectory. Whereas cusps in the grain boundary energy landscape represent energetically favored orientations that are important for faceted pattern formation, local minima in the dissipation energy landscape represent locally favorable shuffling paths that may impact the motion of more general grain boundaries. The cusp

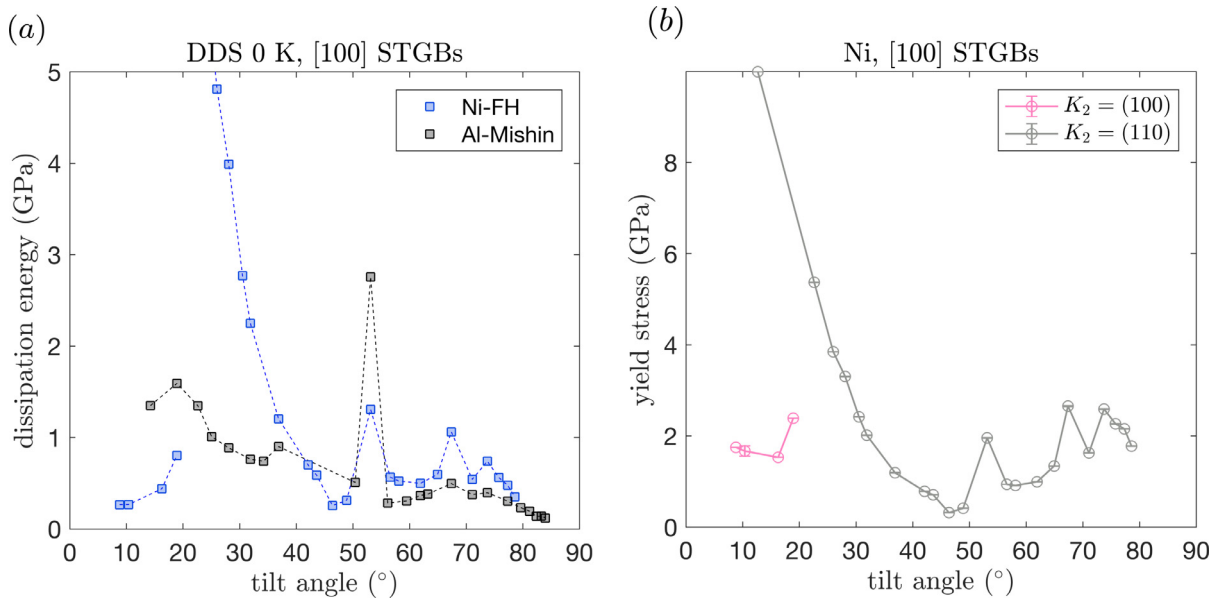


Fig. 8. (a) Dissipation energies for GB motion by shear displacement (DDS) for two EAM potentials. The Al potential only exhibits one coupling mode trajectory ((1 1 0) mode) across the range of surveyed tilt angles. Locations of maxima and minima agree across potential for $\theta > 52^\circ$. (b) Yield surface for motion by shear displacement (DDS). By [example 2](#), the yield surface is a rescaled version of the dissipation energy curve. This rescaling is important for determining cut-off angles for mode switching events.

locations in the grain boundary energy surface are not well correlated with minima in the dissipation energy surface. For instance, the local minimum in the dissipation energy surface at 46.4° does not correspond to a local minimum in the grain boundary energy landscape. We find disagreement in the shape of dissipation energy trajectories for Ni and Al potentials for angles less than 50° . Although the Al dissipation energies generally increase for the (1 1 0) mode, below 50° , the behavior is not monotonic.

DDS and SDF simulations favor different migration modes in the range $22\text{--}35^\circ$, as indicated by disagreement in coupling factors over this window. Shear driven motion favors the high shear (1 1 0) mode even at relatively low tilt angles, consistent with the coupling between shear stress and grain boundary deformation $\mathbf{P} : (\mathbf{F}_{GB}^n - \mathbf{I})$ that is present in the stress and displacement driven, but not energy jump driven case. At angles below 46.4° , the dissipation energy increases monotonically to a large value in excess of 15 GPa at 18.9° . This regime is characterized by an increasing energetic cost of shuffling for large shears, offset by the favorable $\mathbf{P} : (\mathbf{F}_{GB}^n - \mathbf{I})$ coupling term that contributes to mode selection for stress driven motion.

The yield surface for shear strain driven motion ([Fig. 8a](#)) inherits the shape of the dissipation energy curve. However, relative to the DDS dissipation energy curves, high shear data points with large coupling factor are lowered preferentially on the yield surface compared to small shear data points, leading to a shift in critical angle to a lower value than either the DDS or SDF dissipation energy curves. We have insufficient data to determine an exact cutoff point, but note that finite temperature stress driven experiments and molecular dynamics simulations predict a cutoff in the range $30\text{--}35^\circ$ ([Cahn et al., 2006](#); [Gorkaya et al., 2010](#); [2009](#)).

Five grain boundaries driven by an energy jump driving force (SDF) show near zero shear coupling factor in the transition region between (1 0 0) and (1 1 0) modes. Examination of simulation trajectories reveals that vacancies are ejected behind these boundaries as they move. Although this motion mechanism is interesting in its own right for application to radiation damage of grain boundaries [Bai et al. \(2010\)](#); [Han et al. \(2013\)](#); [Li et al. \(2013\)](#), the migration data is inadmissible by our filtering criterion and we denote such boundaries with plotted X symbols.

Detailed analysis of dissipation energy and mode selection results for [1 1 0] and [1 1 1] STGBs are given in [Appendix A](#). For on-mode boundaries, dissipation energies agree closely.

5.2. The need for improved optimization during mode selection in atomistic simulations

The appearance of the (1 0 0) mode in 0 K Ni DDS simulations is, to our knowledge, the first observation of the (1 0 0) mode at 0 K for any interatomic potential.

We observe the (1 0 0) disconnection mode for the Foiles Hoyt Ni potential at 0 K, but do not observe the same mode in Al or Cu interatomic potentials at 0 K. Above 10° , these potentials exhibit the (1 1 0) mode, and below 10° they show a combination of grain boundary sliding and bulk dislocation activity. The absence of the (1 0 0) mode in Cu is consistent with the 0 K results of Mishin and Cahn [Cahn et al. \(2006\)](#); [Deng and Deng \(2019\)](#). Mishin and Cahn state that, for the motion mechanism associated with the (1 0 0) mode in Cu at 0 K, “since the row translations [along the tilt axis] by $1/2[0 0$

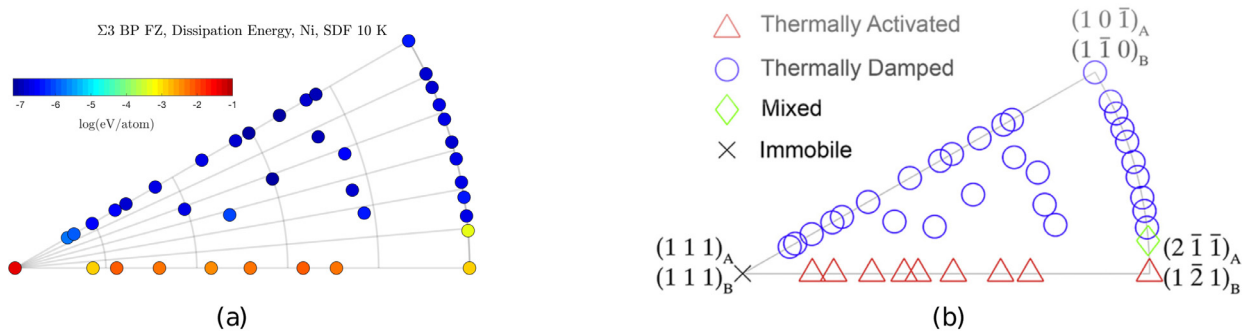


Fig. 9. Dissipation energy and mobility type are correlated. Boundaries that yield easily under an energy jump (low dissipation energy, blue) tend to move more slowly with increasing temperature (thermally damped behavior, blue). Beyond some cutoff dissipation energy, boundaries move in a thermally activated manner. (For interpretation of the references to color in this figure legend, the reader is referred to the web version of this article.) (a) Dissipation energies plotted in $\Sigma 3$ boundary plane fundamental zone on log scale (b) Mobility type classification from Homer survey [Homer, Patala, Priedeman 2015](#).

1] and $1/2[0\ 0\ 1]$ are symmetrically equivalent, this mechanism cannot operate at 0 K" [Cahn et al. \(2006\)](#). The motion of Ni at 0 K in the $(1\ 0\ 0)$ mode suggests a strong dependence of mode selection on small changes in relaxed boundary structure that rely on interatomic potential and the optimization method used to relax the initial boundary structure. In other words, rearrangements of grain boundary structure may break the symmetry mentioned by Mishin and Cahn, even at 0 K.

Frolov has shown that different metastable states of the same crystallographically defined $\Sigma 5(310)$ grain boundary can consistently couple in different modes at finite temperature ([Frolov, 2014](#)). Varying the density of these grain boundary structures was important to observing different modes. Our framework does not currently incorporate dissipation energy spectra arising from multiple metastable states for the same grain boundary. Minimum grain boundary energy does not imply minimum dissipation energy for a given mode, and we expect that more thorough consideration of metastable states, including variable density states, can lead to changes in mode on the yield surfaces for energy jump and stress driven motion. There is an opportunity to develop grain boundary structural optimization algorithms that choose low dissipation energy modes during grain boundary migration simulations.

We note that a possible nonlinear dependence of dissipation energy on driving force may impact mode selection. Dissipation energy may be viewed as an energy barrier to homogeneous disconnection nucleation, as explained further in section 5.6. Combe and Legros studied the dependence of homogeneous disconnection nucleation barriers on stress at 0 K via nudged elastic band (NEB) simulations [Combe et al. \(2016\)](#). Energy barriers were plotted as a function of shear displacement for two atomic displacement trajectories representing the $(1\ 0\ 0)$ and $(1\ 1\ 0)$ mode. It was shown that energy barriers for both modes did not decay linearly to zero with increasing shear displacement. An initial linear decay of the barrier was followed by a sublinear approach to zero energy barrier where yield is expected. Although the $(1\ 0\ 0)$ mode would have been selected by a linear dependence of energy barrier on shear displacement, Combe showed that the $(1\ 1\ 0)$ mode was selected as a result of this nonlinearity. Transition path calculations such as the NEB method should be performed for SDF and DDS displacement trajectories with the same shear coupling mode in order to determine the nonlinear dependence of dissipation energy on shear displacement and synthetic driving force.

5.3. Relationship between dissipation energy, mobility, and temperature

Dissipation energies correlate well with mobility type. Mobility type is a classification for thermal behavior of grain boundaries that describes the sign of change of mobility with increasing temperature. In the original Olmsted mobility survey of 388 GB structures, 15% of the boundaries showed a decrease in mobility with increasing temperature, a phenomenon known as anti-thermal motion ([Homer et al., 2014](#)). A particularly important class of anti-thermal boundaries are twin boundaries with $\Sigma 3$ misorientation and varying boundary plane inclination ([Priedeman et al., 2017](#)). These boundaries show different types of thermal behavior depending on boundary plane inclination, with $[1\ 1\ 0]$ asymmetric tilt boundaries showing thermally activated behavior (red, [Fig. 9b](#)) and most other boundaries showing antithermal behavior (blue, [Fig. 9b](#)) ([Priedeman et al., 2017](#)). Remarkably, dissipation energies computed via SDF simulations at 10 K show a near perfect correlation with mobility type. Low dissipation energies correlate with high mobility, anti-thermal behavior, while high dissipation energies correspond to low mobility, thermally activated boundaries. This correlation is consistent with explicit energy barrier calculations via the GIFE method in ([Chesser and Holm, 2018](#)). Just as yield stress is easier to model than scalar grain boundary mobility, mobility type is more easily predicted than scalar mobility.

At finite temperature, grain boundaries may facet, undergo roughening transitions ([Holm and Foiles, 2010; Olmsted et al., 2007](#)) (described in ([Han et al., 2018](#)) as the simultaneous presence of multiple disconnection modes), or undergo structural transformations. All dissipative mechanisms at finite temperature are sensitive to the rates of change of driving forces. The random walk component of motion due to thermal fluctuations must also be considered ([Ulomek and Mohles, 2016](#)). These factors make correlation of a scalar mobility to low temperature parameters difficult.

Despite the complexity of the general case, we can explore the effect of temperature on dissipation energy using several existing results in the literature for finite temperature DDS simulations. Ivanov, Trautt, and Frolov have surveyed the dependence of yield stress on temperature for several STGBs, demonstrating a decay of yield stress as $T^{2/3}$ with increasing temperature for a single disconnection mode Frolov (2014); Ivanov and Mishin (2008); Trautt et al. (2012). At homologous temperatures of 0.8-0.9, near zero yield stresses are observed associated with grain boundary sliding transitions Cahn et al. (2006) for these boundaries. Dissipation energy can be approximated from these results as yield stress divided by coupling factor. Dissipation therefore saturates to near zero values for these boundaries at high temperatures.

Recent work by Yu and Deng extends the 10 K ramped SDF calculations in this work to a larger temperature range from 100 to 1000 K Yu et al. (2019). Although the dependence of critical driving force on grain boundary geometry and temperature is complex, a correlation is observed between the sign of the change in critical driving force and mobility with temperature. Antithermal boundaries exhibit critical driving forces which apparently increase with temperature, while thermally activated boundaries show critical driving forces which decrease in temperature (similar to the finite T DDS results). Explaining these finite temperature results is out of the scope of the model put forth in this paper, which only considers rate-independent motion in the athermal limit.

5.4. Sources of error for dissipation energy computation

Dissipation energies computed via stress driven motion tend to be smaller than those computed from energy jump driven motion by 0–400 MPa. One possible source of error is the rate dependency of SDF calculations at finite temperature. As shown by Deng in Deng and Deng (2017), high ramp rates overshoot yield stresses and therefore overestimate dissipation energy. In this work, the ramp rates of 10 K SDF simulations were chosen to be sufficiently small to give converged dissipation energies for several boundaries studied in Deng and Deng (2017). A second source of error is the implementation of the synthetic driving force itself. In this work, the Janssens Janssens et al. (2006) implementation was used instead of ECO Ulomek et al. (2015) because of computational efficiency. Ulomek and Mohles showed for a general $\Sigma 7$ boundary Ulomek et al. (2015) that mobilities computed by the Janssens SDF implementation are systematically smaller than those computed by the ECO implementation. This difference in mobilities implies a smaller energy barrier to motion for the Janssens implementation compared to the ECO implementation. Despite this difference, both methods give consistent motion mechanisms and mobility trends with respect to temperature.

5.5. Dependence of dissipation energy on elastic energy difference

Pure shear is an unrealistic stress state for a grain boundary in a real polycrystal, where mixed normal and shear stresses will be resolved upon the boundary (Combe et al., 2017). For specific loading states and grain boundary geometries, an elastic energy difference can contribute to the driving force for grain boundary motion. STGBs loaded under pure shear have no elastic energy difference across the grain boundary. It is shown in Appendix B that normal strains lead to an elastic energy difference for [1 0 0] and [1 1 1] STGBs, but not [1 1 0] STGBs.

Elastic energy difference is incorporated into our continuum thermodynamic framework as an extra term in the yield criterion in Example 2. Elastic energy difference is expressed as $\frac{1}{2}\mathbf{P} : (\mathbb{C}_1^{-1} - \mathbb{C}_2^{-1})\mathbf{P}$, where \mathbb{C}_1 and \mathbb{C}_2 the elastic moduli tensors of the two grains and \mathbf{P} is the applied stress tensor.

Recent work by Deng demonstrates a linear scaling of yield stress with small normal strains applied to the bicrystal for displacement driven motion of [1 0 0] STGBs in Cu (Deng and Deng, 2019). With application of small normal strains in addition to shear displacements, the surveyed grain boundaries have the same coupling factor during all simulations (corresponding to the (1 1 0) mode, in this case). Dissipation energy can be computed by dividing yield stress by coupling factor, implying a linear change in effective dissipation energy with normal strains from compressive strains of -0.03 to tensile strains of 0.05 (Deng and Deng, 2019).

For large normal strains, a nonlinear dependence of yield stress on strain is observed which is associated with a change in grain boundary structure. At sufficiently high normal strains, this change in grain boundary structure can also be accompanied by a change in shear coupling mode (from (1 1 0) to (1 0 0)) (Combe et al., 2017). Our model does not account for this nonlinear regime and associated change in boundary structure.

5.6. Reconciling dissipation energy with other energy barriers as a metric for mode selection

We have defined a dissipation potential which captures rate-independent yield via dissipation energy (ϕ_0^*) and rate-dependent mobility via a higher order dissipation term (ϕ_1^*) that we do not directly model. We have demonstrated that dissipation energy (ϕ_0^*) provides a selection criterion for compatible shear transformations (disconnection modes) independent of driving force in the rate-independent, athermal limit. A correlation between ϕ_0^* and mobility type $\text{sgn}(\frac{\partial \phi_1^*}{\partial T})$ is found. We caution, however, that extending this model to mode selection in the cases of rate-dependency and/or thermal activation does not necessarily follow.

Now we reconcile dissipation energy with disconnection nucleation barriers and activation energies measured in simulations and experiments. Each type of energy barrier is compared in magnitude and as a metric for mode selection. There are

often significant differences in energy barriers measured from experiments and MD simulations. Molodov et. al find activation enthalpies for [1 0 0] symmetric tilt grain boundaries in bicrystal experiments with nominally pure Al that vary little with misorientation angle with an average value of 1.45 eV in the temperature range 280 to 400 ° C (Molodov et al., 2007). Apparently, both motion in the (1 0 0) and (1 1 0) mode corresponds to similar activation enthalpies in these experiments. These values are extracted as the slope of mobility versus temperature profiles. [1 1 0] symmetric tilt grain boundaries were found to have lower activation enthalpies between 0.72-1.09 eV (Brandenburg and Molodov, 2019). Dissipation energies computed in this work vary from 10^{-3} to 0.5 eV/atom and are usually at least an order of magnitude smaller than experimentally measured activation enthalpies. On the other hand, activation energies extracted from mobility versus temperature curves during MD SDF simulations are often quite similar to experimental values (Coleman et al. (2014); Humberson and Holm (2017)). We argue that dissipation energy is a different quantity than activation enthalpy, and that differences in the magnitude of these quantities can be reconciled by considering the impact of temperature, driving force magnitude, and system size on grain boundary motion.

MD simulations of grain boundary migration are frequently overdriven with small system sizes. In this work, driving forces are often on the order of GPa compared to 10 MPa or less in experiments. This pushes grain boundary migration into the “on state,” as is required for energy driven motion at 0 K. In this case, the grain boundary moves uniformly due to the homogeneous nucleation of disconnections loops which quickly join across neighboring periodic boundary conditions. The boundary appears to move up all at once due to coordinated shuffling of atoms. Ulomek proposed that grain boundary migration at finite temperatures can be viewed as a two step process with two energy barriers: a thermally activated initiation step involving long range motion of only a few atoms within the grain boundary and the coordinated shuffling of atoms to move the boundary (Ulomek and Mohles, 2016). By fitting velocity-temperature data for a particular grain boundary driven at 20 MPa, Ulomek showed that the initiation step gives a relatively large energy barrier consistent with experimental activation enthalpy values (though different mechanisms could lead to similar values). The thermally activated initiation step is hypothesized to become increasingly important at small driving forces and low temperatures, whereas the shuffling step is associated with a scalar mobility that is not assumed to obey a thermally activated rate law and dominates at high temperatures. Overall, we find that activation enthalpy values from experiments and MD simulations do not provide an effective metric for mode selection, likely because of competing mechanisms. It may be possible to decouple an energy barrier for shuffling processes similar to dissipation energy from finite temperature simulation trajectories.

Han and Srolovitz have formulated an analytical model for disconnection mode selection based on nucleation controlled disconnection motion (Han et al., 2018). First we elaborate on the term “nucleation controlled.” In the small system size or high driving force limit, disconnection nuclei are very closely spaced across periodic boundary conditions and the boundary migrates nearly uniformly. For large system sizes and lower driving forces, disconnection island structures are observed to reach a critical size before overcoming a nucleation barrier and growing. It is typically assumed that the nucleation barrier is larger than the growth barrier, though these barriers have only been measured via NEB calculations for quasi-2D nucleation in a few flat grain boundaries (Combe et al., 2016). The nucleation barrier is expressed as a competition between the free energy penalty of the disconnection loop (which adds new surface area and defect interactions to the system) and a driving force term. In the model of Han and Srolovitz, an excess enthalpy term for each disconnection (b, h) is proportional to $A|h| + Bb^2$, where A and B are constants that incorporate excess step energy, elastic moduli, disconnection dipole spacing, system size and geometry, and disconnection core size and energy (Han et al. (2018)). Driving force terms $P_{12}b$ and $(u_1 - u_2)h$ are introduced linearly coupling shear stress and an energy jump driving force to the burgers vector and step height component of each disconnection. For certain continuum level assumptions on A and B , mode selection predictions are made for shear coupling factor for symmetric tilt and (1 0 0) asymmetric tilt grain boundaries under constant driving force at 0 K. These predictions largely agree with coupling factors measured at finite temperature in the simulation literature (Chen et al., 2019; Han et al., 2018). Dissipation energy can be considered a lower bound for nucleation energy because it does not take into account the excess energy associated with disconnection island or loop structure. It is a direct atomistic measurement of the shuffling process associated with uniform grain boundary migration that does not make assumptions about grain boundary core structure. Both disconnection nucleation barriers and dissipation energies appear to provide meaningful information about mode selection. Determining the relative magnitude and correlations between the two quantities is the subject of ongoing work.

Dissipation energy is similar to the generalized interfacial fault energy (GIFE) of Barrett et. al in its scale invariant nature. It applies to uniform migration of any flat grain boundary. In the GIFE method, energy barriers to disconnection motion are approximated along uniform shuffling paths during disconnection motion which are linearly interpolated between an initial and final state (Barrett et al. (2017)). The height of these energy barriers are found to correlate with disconnection mode selection in HCP metals. The NEB method may also be used for further relaxation of these trajectories.

Overall, we find it encouraging that dissipation energy gives an energetic argument for disconnection mode selection for multiple driving forces, grain boundary geometries, and boundary conditions that aligns well with existing mode selection data for [1 0 0] STGBs from simulations and experiments. In this work, we have considered flat boundary migration undergoing a single compatible shear transformation. In real polycrystals, a diversity of modes are active across curved grain boundaries, typically at high homologous temperatures where diffusion can play an important role. Network constraints such as triple junctions modify compatibility conditions during grain boundary migration and can couple to crystal plasticity via formation of annealing twins (Thomas et al., 2019). Metrics are needed to correlate atomic rearrangement to boundary structure for a wide range of possible motion mechanisms and grain boundary geometries. We note that dissipation energy can

be interpreted as a special case of “softness,” a generic energy barrier to atomic rearrangement recently defined in machine learning studies on evolution of glass and polycrystalline microstructures during annealing (Sharp et al., 2018). There are many opportunities in extending our continuum framework to multi-mode scenarios.

6. Conclusion

In this work, we have presented a general continuum thermodynamic model for grain boundary motion, and shown that many types of GB behavior can be explained as special cases of this theory. The framework is inspired by previous work on crystal plasticity and the theory of martensitic phase transformations, combined with the constructions of grain boundary shears and dissipation energies. The model is applied to several test examples, verifying that the correct behavior is produced. The key results from this work are that (1) the minimum dissipation potential model captures GB motion for many different driving forces, (2) dissipation potentials are observed to be consistent between loading modes, and (3) they can be used to determine mode selection and shear coupling resulting from an arbitrary driving force in the rate independent, athermal limit. We emphasize that the results of this work are based on the hypothesis that a collection of energy barriers and coupling modes are, collectively, intrinsic grain boundary properties. Our results establish a baseline for understanding low temperature grain boundary migration for a variety of motion mechanisms and loading scenarios in the rate independent limit.

Declaration of Competing Interest

The authors declare that they have no known competing financial interests or personal relationships that could have appeared to influence the work reported in this paper.

Acknowledgments

Work at CMU was supported in part by National Science Foundation grants GFRP-1252522, DMR-1307138, and DMR-1710186, as well as by the W.M. Keck Foundation and the CMU CIT Seed Incubation Program. YT acknowledges support from a scholarship from the Nanjing University of Science and Technology, China. CD acknowledges support from the NSERC Discovery Grant (RGPIN 430800-2013), Canada, and the use of computing resources provided by WestGrid and Compute/Calcul Canada. BR acknowledges computing support from the Extreme Science and Engineering Discovery Environment (XSEDE) allocation TG-PHY130007, which is supported by the National Science Foundation grant number ACI-1548562. Thanks goes to Eric Homer for sharing the Ni grain boundary dataset.

Appendix A. Further analysis of tilt boundaries

The supplementary file [DissipationenergiesSTGB.xlsx](#) contains tabulated values for all dissipation energy values for STGBs.

A.1. $[1\ 1\ 0]$ tilt boundaries

$[1\ 1\ 0]$ tilt boundaries are an important class of grain boundaries with the incoherent $\Sigma 3(112)\|(112)$ and coherent $\Sigma 3(111)\|(111)$ twin boundaries at 70.5° and 109.5° . 15 out of 24 $\langle 1\ 1\ 0 \rangle$ STGBs are filtered out of our analysis corresponding to yield mechanisms that generate bulk dislocation content, leaving 9 admissible data points. Often, inadmissible simulations involve nucleation and extension of shockley partial dislocations into the bulk grains. In contrast to the Ni potential, the Al potential with a higher stacking fault energy gives 12 admissible data points. Since low SFE metals tend to have low barriers for shockley partial nucleation Wang and Huang (2004), we suggest that high stacking fault energy interatomic potentials or BCC elements may be most appropriate for studying disconnection motion in $\langle 1\ 1\ 0 \rangle$ STGBs. We recall that our thermodynamic framework, cast in the language of crystal plasticity, is amenable to implementation in continuum models that consider a wide variety of dissipative mechanisms, including bulk crystal plasticity.

In total, we find only two equal mode $\langle 1\ 1\ 0 \rangle$ STGBs with equivalent shear coupling factors across driving force. These equal mode data point exhibit motion in the $K_2 = (100)$ mode, and are the only SDF data with a non-zero shear coupling factor. Dissipation energies agree within 300 MPa across driving force, consistent with equal mode $\langle 1\ 0\ 0 \rangle$ STGB data. The coherent twin boundary migrates with zero shear coupling factor in SDF simulations, apparently in the zero shear $K_2 = (112)$ mode, but migrates in the $K_2 = (111)$ mode during DDS simulations. In addition to the coherent twin, four other boundaries move in the $(1\ 1\ 1)$ mode during DDS simulations. This mode is not predicted by the Frank Bilby equation, as noted in Homer et al. (2013).

Unlike the Ni potential, the Al potential exhibits a linear regime (defined by three points) tending toward zero dissipation energy at 180° . In addition, at least three shear coupling modes are observed across the range of Al $\langle 1\ 1\ 0 \rangle$ tilt boundaries. Overall, $\langle 1\ 1\ 0 \rangle$ STGBs represent a commonly observed class of boundaries with a zoo of possible dissipative mechanisms and disconnection modes. Successfully modeling the behavior of these boundaries will require incorporating detailed models for grain boundary plasticity into other models for plasticity.

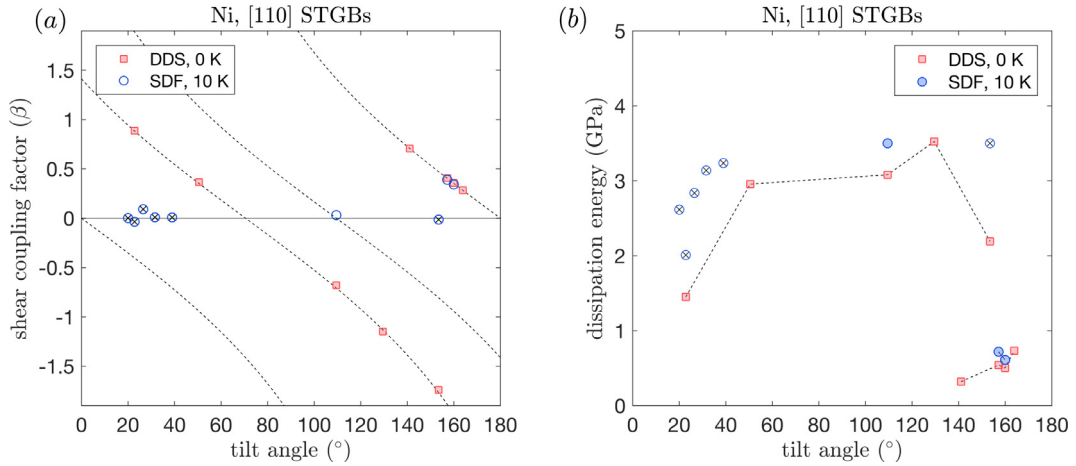


Fig. A.1. (a) Mode selection results for motion via shear displacement (DDS) and energy jump (SDF). Four reference shear coupling trajectories are plotted (from left to right, $K_2 = (100), (111), (112), (110)$). Points with x exhibit a coupling mode with near zero shear that is not consistent with our enumeration scheme (for small shear/height transformations). Unlike results for $(1\ 0\ 0)$ STGBs, points with x involve no additional defect content generated by moving boundary. (b) Dissipation energy trajectories for $(1\ 1\ 0)$ STGBs with consistent modes connected by dashed lines. Only two on mode points may be compared across driving force.

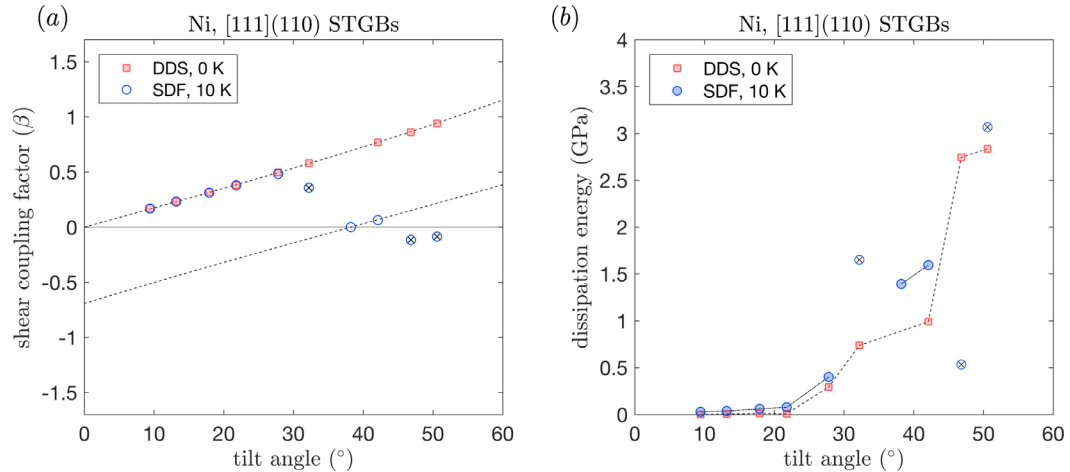


Fig. A.2. (a) Mode selection results for motion via shear displacement (DDS) and energy jump (SDF). Two reference shear coupling trajectories are plotted (from left to right, $K_2 = (110), (145)$). Points with x exhibit a coupling mode that is not consistent with our enumeration scheme (for small shear/height transformations). Unlike results for $(1\ 0\ 0)$ STGBs, points with x involve no additional defect content generated by moving boundary. (b) Dissipation energy trajectories for $[1\ 1\ 1](110)$ STGBs with consistent modes connected by dashed lines. Five on mode points may be compared across driving force.

A.2. $[1\ 1\ 1]$ tilt boundaries

We consider two classes of $\langle 1\ 1\ 1 \rangle$ STGBs: those with zero shear, perfect crystal reference states with $(1\ 1\ 0)$ and $(1\ 1\ 2)$ boundary planes. These two classes, denoted $[1\ 1\ 1](110)$ and $[1\ 1\ 1](112)$, have reference states separated by a rotation of 90° about the $\langle 1\ 1\ 0 \rangle$ tilt axis.

A.2.1. $[1\ 1\ 1](110)$ boundaries

All DDS simulations of $[1\ 1\ 1](110)$ boundaries exhibit the same $(1\ 1\ 0)$ shear coupling mode. SDF simulations deviate from the $(1\ 1\ 0)$ mode at 32° and approach zero. Equal mode boundaries moving in the $(1\ 1\ 0)$ mode are characterized by small dissipation energies on the order of 10 MPa for SDF and 1 MPa for DDS. Small dissipation energies are indicative of fast moving boundaries with easy shuffling transformations. Consistent with LAGB behavior for other tilt axes, dissipation energies approach zero at 0° . This class of boundaries is delimited by the $\Sigma_3(112)\parallel(112)$ incoherent twin boundary at 60° , which is inadmissible. In contrast to the $\langle 1\ 1\ 0 \rangle$ STGB dataset, only two inadmissible datapoints are filtered out of these simulations (the other being DDS at 38.2°). Two boundaries in SDF simulations may couple in the $(1\ 4\ 5)$ mode associated with the $\Sigma_7(231)$ zero shear reference state, though we do not have sufficient data to strengthen this conclusion.

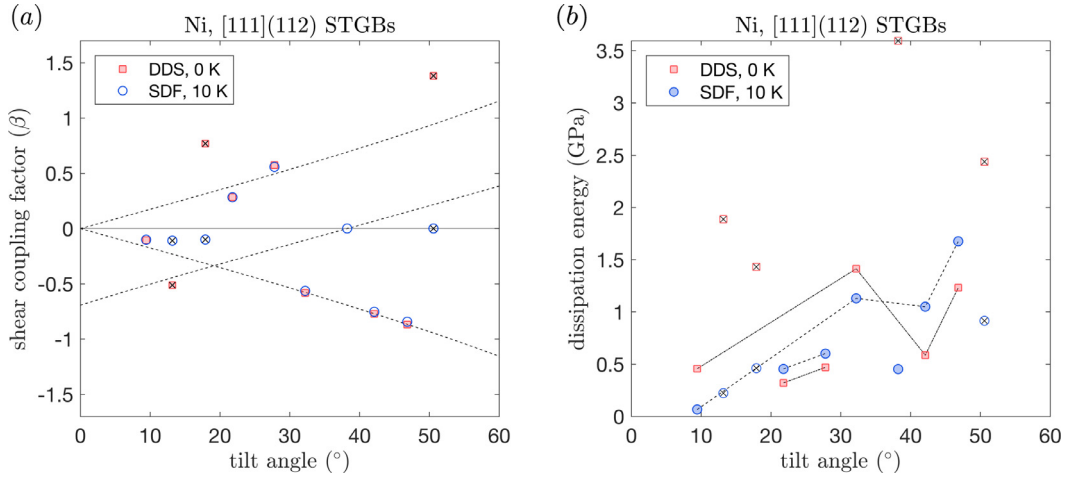


Fig. A.3. (a) Mode selection results for motion via shear displacement (DDS) and energy jump (SDF). Three reference shear coupling trajectories are plotted (left, top and bottom $K_2 = (110)$, (110) and right (231)). Points with x exhibit a coupling mode that is not consistent with our enumeration scheme (for small shear/height transformations). Unlike results for $\langle 1\ 0\ 0 \rangle$ STGBs, points with x involve no additional defect content generated by moving boundary. (b) Dissipation energy trajectories for $[1\ 1\ 1](112)$ STGBs with consistent modes connected by dashed lines. Six on mode points may be compared across driving force.

A.2.2. $[1\ 1\ 1](112)$ boundaries

Whereas the $[1\ 1\ 1](110)$ boundaries are delimited by the $(1\ 1\ 2)$ incoherent twin boundary, the $[1\ 1\ 1](112)$ boundaries are delimited by the $(1\ 1\ 0)$ incoherent twin boundary at 60° . Though the $(1\ 1\ 0)$ twin boundary represents a shallower, higher energy cusp in the GBE landscape than the $(1\ 1\ 2)$ twin boundary, it is one of the most mobile boundaries in the Olmsted survey [Olmsted et al. \(2009b\)](#).

Equal mode boundaries are observed to follow two shear coupling factor trajectories with equal magnitude and opposite sign. This indicates that a symmetric motion mechanism is available to the boundaries, as in the motion of $(1\ 1\ 0)$ twin boundaries during SDF simulations with shuffling vectors along two shockley partial $\langle 1\ 1\ 2 \rangle$ directions [Humberson and Holm \(2017\)](#). Dissipation energies for equal mode boundaries agree within 400 MPa for these boundaries.

In contrast to other boundary sets, $[1\ 1\ 1](110)$ boundaries have several off mode DDS data points with apparently no bulk dislocation content. It is possible that these boundaries include an additional sliding component coupled to grain boundary migration, despite having regular sawtooth stress strain behavior.

Appendix B. Elastic energy difference calculation

In this section we investigate the conditions necessary for an elastically anisotropic bicrystal to exhibit identical response to an applied loading. Recoursing to usual linearized kinematics (in terms of $\boldsymbol{\varepsilon}$), elastic energy U is expressed as

$$U = \frac{1}{2} \boldsymbol{\varepsilon}_{ij} \mathbb{C}_{ijkl} \boldsymbol{\varepsilon}_{kl} \quad (\text{B.1})$$

where \mathbb{C}_{ijkl} is the fourth order elastic modulus tensor and $\boldsymbol{\varepsilon}_{ij}$ a strain tensor in the lab frame. In practice, we usually consider strains $\hat{\boldsymbol{\varepsilon}}_{ij}$ applied in the lattice frame of each grain. We take $\mathbf{R} \in SO(3)$ to be a rotation from the lab frame to the lattice frame such that

$$\boldsymbol{\varepsilon}_{ij} = R_{ip} \hat{\boldsymbol{\varepsilon}}_{pq} R_{qj}^T \quad (\text{B.2})$$

resulting in a transformed expression for elastic energy

$$U = \frac{1}{2} \hat{\boldsymbol{\varepsilon}}_{pq} (R_{ip}^T R_{ks}^T \mathbb{C}_{ijkl} R_{qj} R_{tl}) \hat{\boldsymbol{\varepsilon}}_{st} = \frac{1}{2} \hat{\boldsymbol{\varepsilon}}_{pq} \hat{\mathbb{C}}_{pqst} \hat{\boldsymbol{\varepsilon}}_{st} \quad (\text{B.3})$$

We consider the elasticity tensor for a cubic material. Switching to Voigt notation, \mathbb{C}_{ijkl} is expressed in reduced form as a second order tensor \mathbb{C}_{ij} . Strain is transformed to the voigt strain vector $\boldsymbol{\varepsilon}$

$$\mathbb{C}_{ij} = \begin{pmatrix} C_{11} & C_{12} & C_{12} & 0 & 0 & 0 \\ C_{12} & C_{11} & C_{12} & 0 & 0 & 0 \\ C_{12} & C_{12} & C_{11} & 0 & 0 & 0 \\ 0 & 0 & 0 & C_{44} & 0 & 0 \\ 0 & 0 & 0 & 0 & C_{44} & 0 \\ 0 & 0 & 0 & 0 & 0 & C_{44} \end{pmatrix}, \boldsymbol{\varepsilon}_j = \begin{pmatrix} \varepsilon_{11} \\ \varepsilon_{22} \\ \varepsilon_{33} \\ 2\varepsilon_{23} \\ 2\varepsilon_{31} \\ 2\varepsilon_{12} \end{pmatrix} \quad (\text{B.4})$$

Expressing \mathbb{C} in the lattice frame,

$$\hat{\mathbb{C}}_{ij} = \mathbb{X}\mathbb{C}\mathbb{X}^{-1} \tag{B.5}$$

where \mathbb{X} is a transformation matrix with components

$$\mathbb{X} = \begin{pmatrix} a_{11}^2 & a_{12}^2 & a_{13}^2 & 2a_{12}a_{13} & 2a_{13}a_{11} & 2a_{11}a_{12} \\ a_{21}^2 & a_{22}^2 & a_{23}^2 & 2a_{22}a_{23} & 2a_{23}a_{21} & 2a_{21}a_{22} \\ a_{31}^2 & a_{32}^2 & a_{33}^2 & 2a_{32}a_{33} & 2a_{33}a_{31} & 2a_{31}a_{32} \\ a_{21}a_{31} & a_{22}a_{32} & a_{23}a_{33} & a_{22}a_{33} + a_{23}a_{32} & a_{23}a_{31} + a_{21}a_{33} & a_{21}a_{32} + a_{22}a_{31} \\ a_{31}a_{11} & a_{32}a_{12} & a_{33}a_{13} & a_{32}a_{13} + a_{33}a_{12} & a_{33}a_{11} + a_{31}a_{13} & a_{31}a_{12} + a_{32}a_{11} \\ a_{11}a_{21} & a_{12}a_{22} & a_{13}a_{23} & a_{12}a_{23} + a_{13}a_{22} & a_{13}a_{21} + a_{11}a_{23} & a_{11}a_{22} + a_{12}a_{21} \end{pmatrix} \tag{B.6}$$

where $a_{ij} = \cos(\hat{e}_i, e_j)$.

We suppose that both halves of the bicrystal have equal volume. Then, subject to a strain vector $\boldsymbol{\varepsilon}$ the elastic energy difference is

$$\Delta U = \frac{1}{2} \varepsilon_i (\mathbb{C}_{ij}^2 - \mathbb{C}_{ij}^1) \varepsilon_j \tag{B.7}$$

Therefore, $\ker(\mathbb{C}^2 - \mathbb{C}^1)$ represents all strains that induce no strain energy difference.

Example B.5. ($\langle 100 \rangle$ symmetric tilt) A rotation matrix operator is needed to determine \mathbb{C} for a crystal rotated along the x_1 axis from the laboratory frame. In Voigt notation, the transformation matrix is:

$$\mathbf{R}(\theta) = \begin{bmatrix} \cos^2 \theta & \sin^2 \theta & 0 & 0 & 0 & -2 \sin \theta \cos \theta \\ \sin^2 \theta & \cos^2 \theta & 0 & 0 & 0 & 2 \sin \theta \cos \theta \\ 0 & 0 & 1 & 0 & 0 & 0 \\ 0 & 0 & 0 & \cos \theta & \sin \theta & 0 \\ 0 & 0 & 0 & -\sin \theta & \cos \theta & 0 \\ \sin \theta \cos \theta & -\sin \theta \cos \theta & 0 & 0 & 0 & 2 \cos^2 \theta - 1 \end{bmatrix} \tag{B.8}$$

Then the elastic difference tensor is

$$\mathbb{C}^2 - \mathbb{C}^1 = \mathbf{R}^T(\theta/2) \mathbb{C} \mathbf{R}(\theta/2) - \mathbf{R}^T(-\theta/2) \mathbb{C} \mathbf{R}(-\theta/2) \tag{B.9}$$

Here, let us make the assumption that $2C_{11} - 2C_{12} - C_{44} > 0$ and $0 < \theta < \pi/2$. After considerable algebra, this allows us to express the eigenvalues of $\mathbb{C}^2 - \mathbb{C}^1$ as:

$$\lambda_1 = +\sqrt{2} \cos(\theta) \sin(\theta) (2 \cos(\theta)^2 - 1) (2C_{11} - 2C_{12} - C_{44}) \tag{B.10}$$

$$\lambda_2 = -\sqrt{2} \cos(\theta) \sin(\theta) (2 \cos(\theta)^2 - 1) (2C_{11} - 2C_{12} - C_{44}) \tag{B.11}$$

$$\lambda_3 = \lambda_4 = \lambda_5 = \lambda_6 = 0 \tag{B.12}$$

Corresponding to eigenvectors

$$\mathbf{v}_1 = \begin{bmatrix} -\sqrt{2}/2 \\ \sqrt{2}/2 \\ 0 \\ 0 \\ 0 \\ 1 \end{bmatrix} \quad \mathbf{v}_2 = \begin{bmatrix} \sqrt{2}/2 \\ -\sqrt{2}/2 \\ 0 \\ 0 \\ 0 \\ 1 \end{bmatrix} \quad \mathbf{v}_3, \mathbf{v}_4, \mathbf{v}_5, \mathbf{v}_6 \in (\text{span}\{\mathbf{v}_1, \mathbf{v}_2\})^\perp \tag{B.13}$$

Then the elastic difference for $\mathbf{v}_1, \mathbf{v}_2$ is

$$\Delta U_{100} = -(2C_{11} - 2C_{12} - C_{44}) \varepsilon_{12} (\varepsilon_{11} - \varepsilon_{22}) \sin(2\theta) \tag{B.14}$$

These results prompt the following observations:

1. All eigenvalues are zero for $\theta = n\pi/2$
2. No energy difference for shear in the 2-3 or 1-3 directions
3. Pure shear in the 1-2 direction is zero (eigenvalues cancel out)
4. Signs change if $\theta > \pi/2$ or $\theta < 0$, and eigenvectors are undefined when eigenvalues are zero.
5. Combination of tension/compression in the 1-1 and 2-2 directions and shear in the 1-2 direction leads to nonzero elastic energy difference

Example B.6. ((110)symmetric tilt) Making the same assumptions as before, we consider as the transformation tensor the Voigt rotation matrix about a $\langle 1\ 1\ 0 \rangle$ axis. Proceeding as above gives eigenvalues of $\mathbb{C}^2 - \mathbb{C}^1$ with the following relationships:

$$\lambda_1 = \lambda_2 = 0 \quad (\text{B.15})$$

$$\lambda_3 = -\lambda_4 \quad (\text{B.16})$$

$$\lambda_5 = -\lambda_6 \quad (\text{B.17})$$

The eigenvalues and eigenvectors have cumbersome expressions that depend on θ and are excluded here for brevity. The calculated elastic energy difference is

$$\Delta U_{110} = \frac{\sin(\theta)}{4\sqrt{2}} (2C_{11} - 2C_{12} - C_{44}) (5\varepsilon_{11}\varepsilon_{13} + 12\varepsilon_{12}\varepsilon_{13} + 3\varepsilon_{11}\varepsilon_{23} - 3\varepsilon_{13}\varepsilon_{22} - 5\varepsilon_{22}\varepsilon_{23} - 2\varepsilon_{13}\varepsilon_{33}) \quad (\text{B.18})$$

$$+ 2\varepsilon_{23}\varepsilon_{33} + 3(\varepsilon_{13} - \varepsilon_{23})(\varepsilon_{11} - 4\varepsilon_{12} + \varepsilon_{22} - 2\varepsilon_{33}) \cos(\theta) \quad (\text{B.19})$$

We make the following notes about these results:

1. All eigenvalues are zero for $\theta = n\pi$
2. No energy difference for strains with only one component, including pure shear in the 1–2 direction
3. No energy difference for shear in the 1–2 direction combined with normal strains
4. Energy difference for shear in the 1–2 direction with nonzero shear strains in 1–3 or 2–3 direction. Elastic energy difference vs. tilt angle curves are asymmetric and unimodal about $\theta = \pi/2$ for combinations of shear strains. With addition of normal strains, elastic energy difference may change sign at an intermediate tilt angle.
5. Energy difference for shear in the 1–3 or 2–3 direction only with normal strains. Appropriately chosen parameters can once again lead to sign change in elastic energy vs. tilt angle curves.

Example B.7. ((111)symmetric tilt) Using the voigt rotation matrix about a $\langle 1\ 1\ 1 \rangle$ axis and proceeding as above, we find eigenvalues of $\mathbb{C}^2 - \mathbb{C}^1$ with the following relationships:

$$\lambda_1 = \lambda_2 = -\frac{2}{3} (2C_{11} - 2C_{12} - C_{44}) \sin\left(\frac{3\theta}{2}\right) \quad (\text{B.20})$$

$$\lambda_3 = \lambda_4 = +\frac{2}{3} (2C_{11} - 2C_{12} - C_{44}) \sin\left(\frac{3\theta}{2}\right) \quad (\text{B.21})$$

$$\lambda_5 = \lambda_6 = 0 \quad (\text{B.22})$$

The eigenvectors do not depend on θ . Note that this is true for the $\langle 1\ 0\ 0 \rangle$ case but not the $\langle 1\ 1\ 0 \rangle$ case. The elastic energy difference is

$$\Delta U_{111} = \frac{4 \sin(3\theta/2)}{3\sqrt{3}} (2C_{11} - 2C_{12} - C_{44}) (\varepsilon_{11}(\varepsilon_{12} - \varepsilon_{13}) - \varepsilon_{12}\varepsilon_{22} + \varepsilon_{22}\varepsilon_{23} + \varepsilon_{13}\varepsilon_{33} - \varepsilon_{23}\varepsilon_{33}) \quad (\text{B.23})$$

We note the following about the results:

1. All eigenvalues are zero for $\theta = n\frac{2\pi}{3}$
2. No energy difference for strains with only one component, including pure shear in the 1–2 direction
3. Energy difference for shear in the 1–2 direction combined with normal strains in the 1-1 or 2-2 direction, or combination of shear along 1–3 with normal strains in 1-1,2-2, or shear along 2–3 with normal strains 2-2 and 3-3.

Summary

For the $\langle 1\ 1\ 1 \rangle$ and $\langle 1\ 0\ 0 \rangle$ tilt axes (three and four fold symmetry about tilt axis): combinations of shear and normal strains lead to an elastic energy difference. Elastic energy difference vs. tilt angle curves are symmetric for all combinations of strains. The overall elastic energy difference curve may change sign with a change in relative amounts of strain.

For the $\langle 1\ 1\ 0 \rangle$ tilt axes (two fold symmetry about tilt axis): Unlike the other cases the eigenvectors of elastic modulus difference tensor depend on tilt angle. The shape of the elastic energy v. tilt angle curves may lose symmetry about the midpoint angle or change sign at some intermediate tilt angle for an appropriately chosen set of strains. Like the $\langle 1\ 0\ 0 \rangle$ case, variations in strain may lead to a sign flip of the entire curve. A shear along the 1–2 direction leads to an elastic energy difference only in combination with other shear strains.

Supplementary material

Supplementary material associated with this article can be found, in the online version, at doi:10.1016/j.jmps.2019.103827.

References

- Bai, X.-M., Voter, A.F., Hoagland, R.G., Nastasi, M., Uberuaga, B.P., 2010. Efficient annealing of radiation damage near grain boundaries via interstitial emission. *Science* 327 (5973), 1631–1634.
- Ball, J.M., 2004. Mathematical models of martensitic microstructure. *Mater. Sci. Eng. A* 378 (1–2), 61–69.
- Ball, J.M., James, R.D., 1989. Fine phase mixtures as minimizers of energy. In: *Analysis and Continuum Mechanics*. Springer, pp. 647–686.
- Barrett, C.D., El Kadiri, H., Moser, R., 2017. Generalized interfacial fault energies. *Int. J. Solid. Struct.* 110, 106–112.
- Brandenburg, J.-E., Molodov, D.A., 2019. On shear coupled migration of low angle grain boundaries. *Scripta Materialia* 163, 96–100.
- Cahn, J., Mullins, W., 1962. Decomposition of austenite by diffusional processes. *InterScience* 123.
- Cahn, J.W., Mishin, Y., Suzuki, A., 2006. Coupling grain boundary motion to shear deformation. *Acta materialia* 54 (19), 4953–4975.
- Cantwell, P.R., Holm, E.A., Harmer, M.P., Hoffmann, M.J., 2015. Anti-thermal behavior of materials. *Scripta Materialia* 103, 1–5.
- Carstensen, C., Hackl, K., Mielke, A., 2001. Non-convex potentials and microstructures in finite-strain plasticity. *Proceed. Roy. Soc. Lond. Ser. A* 458 (2018), 299–317.
- Chen, K., Han, J., Thomas, S.L., Srolovitz, D.J., 2019. Grain boundary shear coupling is not a grain boundary property. *Acta Materialia* 167, 241–247.
- Chesser, I., Holm, E., 2018. Understanding the anomalous thermal behavior of $\sigma 3$ grain boundaries in a variety of fcc metals. *Scripta Materialia* 157, 19–23.
- Chookajorn, T., Murdoch, H.A., Schuh, C.A., 2012. Design of stable nanocrystalline alloys. *Science* 337 (6097), 951–954.
- Coleman, B.D., Noll, W., 1974. The thermodynamics of elastic materials with heat conduction and viscosity. In: *The Foundations of Mechanics and Thermodynamics*. Springer, pp. 145–156.
- Coleman, S.P., Spearot, D.E., Foiles, S.M., 2014. The effect of synthetic driving force on the atomic mechanisms associated with grain boundary motion below the interface roughening temperature. *Comput. Mater. Sci.* 86, 38–42.
- Combe, N., Momprou, F., Legros, M., 2016. Disconnections kinks and competing modes in shear-coupled grain boundary migration. *Phys. Rev. B* 93, 024109. doi:10.1103/PhysRevB.93.024109.
- Combe, N., Momprou, F., Legros, M., 2017. Shear-coupled grain-boundary migration dependence on normal strain/stress. *Phys. Rev. Mater.* 1 (3), 33605.
- Deng, Y., Deng, C., 2017. Size and rate dependent grain boundary motion mediated by disconnection nucleation. *Acta Materialia* 131, 400–409.
- Deng, Y., Deng, C., 2019. Atomic link between the structure and strength of grain boundaries subject to shear coupling. *Phys. Rev. Mater.* 3 (1), 10601.
- Erickson, J.L., 2008. On the Cauchy-Born rule. *Math. Mech. Solid.* 13 (3–4), 199–220.
- Foiles, S.M., Hoyt, J., 2006. Computation of grain boundary stiffness and mobility from boundary fluctuations. *Acta Materialia* 54 (12), 3351–3357.
- Frolov, T., 2014. Effect of interfacial structural phase transitions on the coupled motion of grain boundaries: a molecular dynamics study. *Appl. Phys. Lett.* 104 (21), 211905.
- Gorkaya, T., Burlet, T., Molodov, D.A., Gottstein, G., 2010. Experimental method for true in situ measurements of shear-coupled grain boundary migration. *Scripta Materialia* 63 (6), 633–636.
- Gorkaya, T., Molodov, D.A., Gottstein, G., 2009. Stress-driven migration of symmetrical $\langle 1\ 0\ 0 \rangle$ tilt grain boundaries in Al bicrystals. *Acta Materialia* 57 (18), 5396–5405.
- Gottstein, G., Shvindlerman, L.S., 2009. *Grain Boundary Migration in Metals: Thermodynamics, Kinetics, Applications*. CRC press.
- Grippo, L., Lucidi, S., 1997. A globally convergent version of the Polak-Ribiere conjugate gradient method. *Math. Program.* 78 (3), 375–391.
- Hackl, K., Fischer, F.D., 2008. On the relation between the principle of maximum dissipation and inelastic evolution given by dissipation potentials. In: *Proceedings of the Royal Society of London A: Mathematical, Physical and Engineering Sciences*, 464. The Royal Society, pp. 117–132.
- Hackl, K., Kochmann, D.M., 2008. Relaxed potentials and evolution equations for inelastic microstructures. In: *IUTAM Symposium on Theoretical, Computational and Modelling Aspects of Inelastic Media*. Springer, pp. 27–39.
- Han, J., Thomas, S. L., Srolovitz, D. J., 2018. Grain-boundary kinetics: a unified approach 98, 386–476.
- Han, W., Demkowicz, M.J., Mara, N.A., Fu, E., Sinha, S., Rollett, A.D., Wang, Y., Carpenter, J.S., Beyerlein, I.J., Misra, A., 2013. Design of radiation tolerant materials via interface engineering. *Adv. Mater.* 25 (48), 6975–6979.
- Hillert, M., Ågren, J., 2006. Extremum principles for irreversible processes. *Acta Materialia* 54 (8), 2063–2066.
- Hirth, J.P., 1994. Dislocations, steps and disconnections at interfaces. *J. Phys. Chem. Solid.* 55 (10), 985–989. doi:10.1016/0022-3697(94)90118-X.
- Holm, E.A., Foiles, S.M., 2010. How grain growth stops: a mechanism for grain-growth stagnation in pure materials. *Science* 328 (5982), 1138–1141.
- Homer, E.R., Foiles, S.M., Holm, E.A., Olmsted, D.L., 2013. Phenomenology of shear-coupled grain boundary motion in symmetric tilt and general grain boundaries. *Acta Materialia* 61 (4), 1048–1060.
- Homer, E.R., Holm, E.A., Foiles, S.M., Olmsted, D.L., 2014. Trends in grain boundary mobility: survey of motion mechanisms. *Jom* 66 (1), 114–120.
- Homer, E.R., Patala, S., Priedeman, J.L., 2015. Grain boundary plane orientation fundamental zones and structure-property relationships. *Sci. Rep.* 5, 15476.
- Humberson, J., Holm, E.A., 2017. Anti-thermal mobility in the $\sigma 3$ [111] (11 8 5) grain boundary in nickel: mechanism and computational considerations. *Scripta Materialia* 130, 1–6.
- Ivanov, V., Mishin, Y., 2008. Dynamics of grain boundary motion coupled to shear deformation: an analytical model and its verification by molecular dynamics. *Phys. Rev. B* 78 (6), 64106.
- Janssens, K.G., Olmsted, D., Holm, E.A., Foiles, S.M., Plimpton, S.J., Derlet, P.M., 2006. Computing the mobility of grain boundaries. *Nat. Mater.* 5 (2), 124.
- Jin, S., Huang, M., Kwon, Y., Zhang, L., Li, B.-W., Oh, S., Dong, J., Luo, D., Biswal, M., Cunniff, B.V., et al., 2018. Colossal grain growth yields single-crystal metal foils by contact-free annealing. *Science* 362 (6418), 1021–1025.
- Kochmann, D.M., Hackl, K., 2011. The evolution of laminates in finite crystal plasticity: a variational approach. *Cont. Mech. Thermodyn.* 23 (1), 63–85.
- Li, C.H., Edwards, E.H., Washburn, J., Parker, E.R., 1953. Stress-induced movement of crystal boundaries. *Acta Metallurgica* 1 (2), 223–229.
- Li, N., Wang, J., Wang, Y., Serruys, Y., Nastasi, M., Misra, A., 2013. Incoherent twin boundary migration induced by ion irradiation in Cu. *J. Appl. Phys.* 113 (2), 23508.
- Martyshev, L.M., Seleznev, V.D., 2006. Maximum entropy production principle in physics, chemistry and biology. *Phys. Rep.* 426 (1), 1–45.
- Meyers, M.A., Mishra, A., Benson, D.J., 2006. Mechanical properties of nanocrystalline materials. *Prog. Mater. Sci.* 51 (4), 427–556.
- Mielke, A., 2002. Finite elastoplasticity lie groups and geodesics on $sl(d)$. In: *Geometry, mechanics, and dynamics*. Springer, pp. 61–90.
- Mielke, A., Ortiz, M., 2008. A class of minimum principles for characterizing the trajectories and the relaxation of dissipative systems. *ESAIM* 14 (3), 494–516.
- Mishin, Y., Mehl, M., Papaconstantopoulos, D., Voter, A., Kress, J., 2001. Structural stability and lattice defects in copper: ab initio, tight-binding, and embedded-atom calculations. *Phys. Rev. B* 63 (22), 224106.
- Mishin, Y., Suzuki, A., Uberuaga, B., Voter, A., 2007. Stick-slip behavior of grain boundaries studied by accelerated molecular dynamics. *Phys. Rev. B* 75 (22), 224101.
- Molodov, D., Ivanov, V., Gottstein, G., 2007. Low angle tilt boundary migration coupled to shear deformation. *Acta Materialia* 55 (5), 1843–1848.
- Molodov, K.D., Molodov, D.A., 2018. Grain boundary mediated plasticity: on the evaluation of grain boundary migration-shear coupling. *Acta Materialia* 153, 336–353.
- Momprou, F., Legros, M., Caillard, D., 2010. Smig model: a new geometrical model to quantify grain boundary-based plasticity. *Acta Materialia* 58 (10), 3676–3689.

- Olmsted, D.L., Foiles, S.M., Holm, E.A., 2007. Grain boundary interface roughening transition and its effect on grain boundary mobility for non-faceting boundaries. *Scripta Materialia* 57 (12), 1161–1164.
- Olmsted, D.L., Foiles, S.M., Holm, E.A., 2009. Survey of computed grain boundary properties in face-centered cubic metals: i. grain boundary energy. *Acta Materialia* 57 (13), 3694–3703.
- Olmsted, D.L., Holm, E.A., Foiles, S.M., 2009. Survey of computed grain boundary properties in face-centered cubic metals ii: grain boundary mobility. *Acta Materialia* 57 (13), 3704–3713.
- Onsager, L., 1931. Reciprocal relations in irreversible processes. i. *Phys. Rev.* 37 (4), 405.
- Ortiz, M., Repetto, E., 1999. Nonconvex energy minimization and dislocation structures in ductile single crystals. *J. Mech. Phys. Solid.* 47 (2), 397–462.
- Pedrazas, N.A., Buchheit, T.E., Holm, E.A., Taleff, E.M., 2014. Dynamic abnormal grain growth in tantalum. *Mater. Sci. Eng. A* 610, 76–84.
- Pitteri, M., Zanzotto, G., 2002. Continuum Models for Phase Transitions and Twinning in Crystals. Chapman and Hall/CRC.
- Plimpton, S., 1995. Fast parallel algorithms for short-range molecular dynamics. *J. Comput. Phys.* 117 (1), 1–19.
- Priedeman, J.L., Olmsted, D.L., Homer, E.R., 2017. The role of crystallography and the mechanisms associated with migration of incoherent twin grain boundaries. *Acta Materialia* 131, 553–563.
- Raabe, D., Lücke, K., 1992. Texture and microstructure of hot rolled steel. *Scripta Metallurgica* 26, 1221–1226.
- Race, C.P., Hadian, R., von Pezold, J., Grabowski, B., Neugebauer, J., 2015. Mechanisms and kinetics of the migration of grain boundaries containing extended defects. *Phys. Rev. B* 92 (17), 174115.
- Rollett, A., Gottstein, G., Shvindlerman, L., Molodov, D., 2004. Grain boundary mobility—a brief review. *Zeitschrift für Metallkunde* 95 (4), 226–229.
- Rollett, A., Humphreys, F., Rohrer, G., Hatherly, M., 2004. Recrystallization and Related Annealing Phenomena. 2004. Elsevier.
- Roubíček, T., 2009. Rate-independent processes in viscous solids at small strains. *Math. Method. Appl. Sci.* 32 (7), 825–862.
- Roubíček, T., 2010. Thermodynamics of rate-independent processes in viscous solids at small strains. *SIAM J. Math. Anal.* 42 (1), 256–297.
- Rupert, T., Gianola, D., Gan, Y., Hemker, K., 2009. Experimental observations of stress-driven grain boundary migration. *Science* 326 (5960), 1686–1690.
- Sharp, T.A., Thomas, S.L., Cubuk, E.D., Schoenholz, S.S., Srolovitz, D.J., Liu, A.J., 2018. Machine learning determination of atomic dynamics at grain boundaries. *Proceedi. Natl. Acad. Sci.* 115 (43), 10943–10947.
- Shi, F., Tian, P., Jia, N., Ye, Z., Qi, Y., Liu, C., Li, X., 2016. Improving intergranular corrosion resistance in a nickel-free and manganese-bearing high-nitrogen austenitic stainless steel through grain boundary character distribution optimization. *Corr. Sci.* 107, 49–59.
- Sun, D., Ponga, M., Bhattacharya, K., Ortiz, M., 2018. Proliferation of twinning in hexagonal close-packed metals: application to magnesium. *J. Mech. Phys. Solid.* 112, 368–384.
- Thomas, S.L., Chen, K., Han, J., Purohit, P.K., Srolovitz, D.J., 2017. Reconciling grain growth and shear-coupled grain boundary migration. *Nat. Commun.* 8 (1), 1764.
- Thomas, S.L., Wei, C., Han, J., Xiang, Y., Srolovitz, D.J., 2019. Disconnection description of triple-junction motion. *Proceedi. Natl. Acad. Sci.* 201820789.
- Trautt, Z., Adland, A., Karma, A., Mishin, Y., 2012. Coupled motion of asymmetrical tilt grain boundaries: molecular dynamics and phase field crystal simulations. *Acta Materialia* 60 (19), 6528–6546.
- Tschopp, M., McDowell, D., 2007. Asymmetric tilt grain boundary structure and energy in copper and aluminium. *Philos. Mag.* 87 (25), 3871–3892.
- Ulomek, F., Mohles, V., 2016. Separating grain boundary migration mechanisms in molecular dynamics simulations. *Acta Materialia* 103, 424–432.
- Ulomek, F., O'Brien, C., Foiles, S., Mohles, V., 2015. Energy conserving orientational force for determining grain boundary mobility. *Model. Simul. Mater. Sci. Eng.* 23 (2), 25007.
- Wang, J., Huang, H., 2004. Shockley partial dislocations to twin: another formation mechanism and generic driving force. *Appl. Phys. Lett.* 85 (24), 5983–5985.
- Worthington, D.L., Pedrazas, N.A., Noell, P.J., Taleff, E.M., 2013. Dynamic abnormal grain growth in molybdenum. *Metall. Mater. Trans. A* 44 (11), 5025–5038.
- Yin, J., Wang, Y., Yan, X., Hou, H., Wang, J.T., 2018. Atomistic simulation of shear-coupled motion of [1 1 0] symmetric tilt grain boundary in α -iron. *Comput. Mater. Sci.* 148, 141–148.
- Yu, T., Yang, S., Deng, C., 2019. Survey of grain boundary migration and thermal behavior in ni at low homologous temperatures. *Acta Materialia*.
- Zamberger, S., Whitmore, L., Krisam, S., Wojcik, T., Kozeschnik, E., 2015. Experimental and computational study of cementite precipitation in tempered martensite. *Model. Simul. Mater. Sci. Eng.* 23 (5), 55012.
- Zhang, H., Mendelev, M., Srolovitz, D., 2004. Computer simulation of the elastically driven migration of a flat grain boundary. *Acta materialia* 52 (9), 2569–2576.